INVESTIGATION OF AN UNDERWATER ELECTROMAGNETIC COMMUNICATIONS CHANNEL

BY

DOUGLAS WESCOTT WHITE
S.B.
MASSACHUSETTS INSTITUTE OF TECHNOLOGY
1975

SUBMITTED IN PARTIAL FULFILLMENT
OF THE REQUIREMENTS FOR THE
DEGREES OF

MASTER OF SCIENCE
AND
ELECTRICAL ENGINEER
AT THE
MASSACHUSETTS INSTITUTE OF TECHNOLOGY
JANUARY 1978

SIGNATURE OF AUTHOR .....
DEPARTMENT OF ELECTRICAL ENGINEERING AND COMPUTER SCIENCE
JANUARY 20, 1978

CERTIFIED BY .....
THESIS SUPERVISOR (M.I.T.)

CERTIFIED BY .....
THESIS SUPERVISOR (W.H.O.I.)

ACCEPTED BY .....
CHAIRMAN, DEPARTMENTAL COMMITTEE ON GRADUATE STUDENTS

INVESTIGATION OF AN UNDERWATER ELECTROMAGNETIC COMMUNICATIONS CHANNEL

by

DOUGLAS WESCOTT WHITE

Submitted to the Department of
Electrical Engineering and Computer Science
on January 20, 1978
in partial fulfillment of the
requirements for the Degrees of
Master of Science and Electrical Engineer

ABSTRACT

Although underwater electromagnetic signals attenuate rapidly with distance, especially above audio frequencies, the presence of the ocean surface can reduce this attenuation a great deal in some cases. To investigate the use of electromagnetic signals for short-range broad-band communication, the propagation of such signals, and the noise environment in the ocean were studied.

The signal attenuation from a submerged source transmitting vertically to a receiver near the surface was calculated using a numerical integration computer program and was then measured experimentally. The fit between the theory and the data is quite good, although the measured signal was always slightly stronger than predicted. The field attenuates very rapidly with distance and increasing frequency.

The electrical noise in the ocean between 1 and 100 kHz consists of a background level which decreases slowly with increasing frequency, and a number of strong narrow-band sources of unknown origin. Estimates of the channel capacity indicate that the signal attenuation at increasing frequencies is sufficient to limit the possibility of broad-band signal transmission underwater severely.

Another phenomenon investigated is a shift in the relative strengths of the field components of a submerged dipole near the surface. Although there was some discrepancy between the experimental results and the theory, the effect appears to be real, and may have applications in measuring the conductivity of sea water.

In general, the results indicate that this form of communication has a number of severe limitations. Except in cases where the acoustic noise is extremely bad, an acoustic communications system will probably have greater range and bandwidth for the same transmitted power.

THESIS SUPERVISORS

A. B. Baggeroer, Associate Professor of Electrical Engineering, M.I.T.

A. M. Bradley, Research Associate, Woods Hole Oceanographic Institution

TABLE OF CONTENTS

LIST OF FIGURES

ACKNOWLEDGEMENTS

I would like to thank the many friends who assisted with the experiments, the people of the Ocean Engineering Department at the Woods Hole Oceanographic Institution for their friendly advice and generous loans of equipment, and the professors at M.I.T. and Harvard who gave me technical advice. I am especially grateful to my two thesis advisors, Dr. Albert Bradley of W.H.O.I. and Professor Arthur Baggeroer of M.I.T., for their assistance throughout this work.

CHAPTER 1

INTRODUCTION

The use of electromagnetic fields for underwater communication has been investigated almost since the discovery of normal radio communications. The French used electromagnetic signals to communicate with submarines during the First World War, and they have been used for that purpose, in one form or another, ever since. Short range communication with divers was investigated during World War II by the U.S. Office of Scientific Research and Development.[1]

More recently, increasing oceanographic research, commercial underwater endeavor, and sport diving have added to the need for reliable underwater communications. In addition to government sponsored researchers, several companies have worked on the problem of using electromagnetic fields as a means of communication, and even a few Amateur Radio enthusiasts have experimented with it.[2] In the past few years, two commercial firms have developed systems, one for short range diver communication,[3] and the other for an instrument release system.[4]

Theoretical analysis of the problem is quite complex, and over a hundred papers treating the problem in one form or another have been written since 1909 when Sommerfeld first studied the fields of an antenna at the air-sea interface. The presence of the surface is critical to the problem, a fact which many experimenters have failed to realize.

When both the transmitting and receiving antennas are submerged in an infinite conducting medium, radiation of plane waves decays exponentially with distance, severely limiting the practical range except at extremely low frequencies where the exponential decay is slowest. This is the cause of the widespread belief that electromagnetic communications underwater is a "dead end" if long range or large bandwidth communications are desired. This type of attenuation also occurs when waves are incident on the surface, and this is the reason for the low frequencies which are currently being investigated for communication from the shore to submerged submarines. The navy has done a great deal of research in the last fifteen years on Extremely Low Frequency (ELF) transmission in the frequency range of 30 to 300 hertz. Signals at these frequencies penetrate quite deeply into the water, and the low frequencies allow excitation of the space between the earth and the ionosphere as a form of resonant cavity to increase the signal strength.[5,6]

If both the transmitter and receiver are submerged, but close to the surface, a "surface wave" mode of propagation, similar to "head" wave propagation found in seabed acoustics, becomes very important. Depending on the parameters involved (depth, frequency, range, etc.), a large portion of the signal propagates from the transmitter up through the water, along the surface, and then down to the receiver. Under proper conditions, the attenuation of the signal goes only as one over the distance cubed, rather than as a decaying exponential.

This surface wave phenomenon has been the focus of a great deal of theoretical work on the problem, and considerable amount of

discussion in the literature for many years was centered around whether or not the effect was real at all. The effects of the surface on transmission are also responsible for a number of experimenters' claims of transmissions at a fraction of a watt over distances of 100 meters or more.

The O.S.R.D. research during World War II concluded that underwater communication with electromagnetic signals was quite practical over moderate distances. The field attenuation they measured matches with the inverse cube relationship predicted by current theory for transmission near the surface, although the theoretical equations they presented (but did not derive in their paper) predicted this behavior for any depth. Because the measurements they made near the surface matched their calculations, they predicted that the system would work just as well regardless of the proximity of the surface.

During the mid-1960's, the problem was brought to public attention by a chemist, W. Minto, in a number of articles in popular magazines claiming to have discovered an entirely new form of communication.[7] Because he had measured signals considerably stronger than any exponential attenuation could have produced, (presumably by transmitting near the surface), he believed that it could only be some form of propagation other than electromagnetic waves, and he made a number of wild claims about revolutionizing underwater communications.[8] The articles stopped rather abruptly, and nothing about his "new" communication scheme has been published since.

Interest in Minto's claims inspired the research leading to the

Bachelor's thesis "Investigation of an Electromagnetic Underwater Communications System."[9] Preliminary research was done to study the effect of the surface on the field of a submerged short dipole antenna. Several experiments were performed, but with rather inconclusive results. This thesis is a continuation of that work.

Since 1975, further research into the literature produced a detailed theoretical analysis of the surface problem using saddle point methods to find asymptotic solutions to the field equations.[10] Several recent works have used numerical integration techniques and experimental results to verify and expand on the results of the saddle point analysis.[11,12,13]

One interesting result of the saddle point analysis which had not been carefully investigated is the apparent "rotation" of the dipole field near the surface. For a regular dipole field, the peak radial component is twice as strong as the peak azimuthal component. The theoretical calculations using saddle point techniques for the fields near the surface (at moderate ranges) indicate that the *azimuthal* component is twice as strong as the radial component (see Figure 1.1).

As part of the current thesis work, a transmitter and receiver were constructed, and measurements comparing the two field components were taken. Equations for the two field components at short ranges were derived for the case of the antennas located at the surface, and the results were compared with the experimental data.

For the range of frequencies of interest (one to one hundred kilohertz), the saddle point method breaks down for the case of

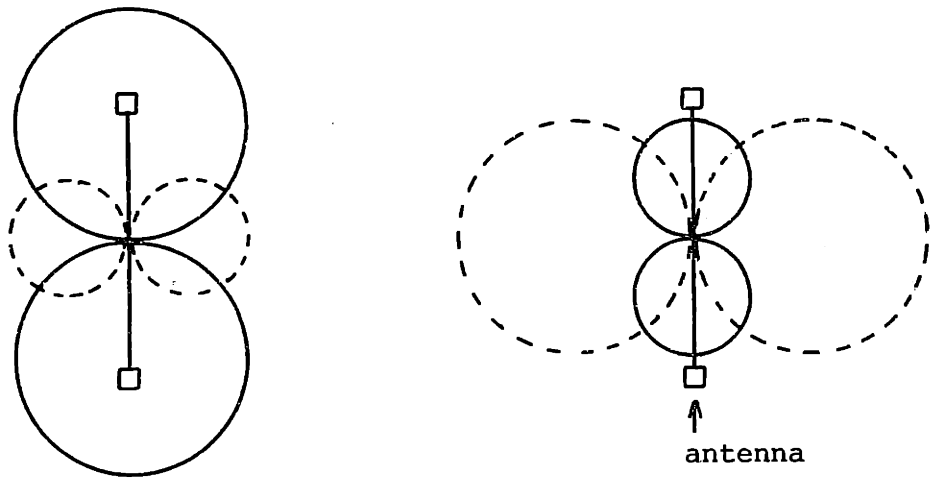

FIGURE 1.1
RELATIVE FIELD STRENGTH PATTERNS

transmission near the vertical axis, and all of the numerical and experimental efforts until now have concentrated on the region near the surface where the surface wave phenomenon is important. Although perhaps not as scientifically interesting a problem as the surface case, this is the most important mode for a great deal of practical oceanographic work.

To investigate vertical transmission from a submerged transmitter to a receiver near the surface, a computer program was developed to numerically evaluate the electric field equation. Experimental measurements of the vertical field attenuation were taken

to compare with the numerical results. The tests were performed using a 100 kHz waterproof transmitter and the receiver developed for the surface field experiments.

Another area of practical interest which has not been thoroughly investigated is that of the ambient electrical noise in the ocean at audio frequencies. If a great deal of the noise is caused by distant sources, such as electrical storms, then the high frequencies will be attenuated in the same way as the transmitted signal's high frequency components. It may be possible to take advantage of this sort of constant signal-to-noise property to develop a practical communications system. For this reason, an evaluation of the typical noise levels at various frequencies could be very useful. Once the characteristics of the noise are known, quantities such as the channel capacity can be calculated to evaluate the information-handling capabilities of this type of communications system.

A low-noise preamplifier was constructed, and measurements of the noise spectrum in the water were taken at several different depths and antenna orientations. These results were then compared with the frequency characteristics of the transmission system (calculated using the computer program developed for the vertical field case), and estimates of the channel capacity were calculated from Shannon's channel capacity theorem.

CHAPTER 2

THEORETICAL BACKGROUND

The theoretical problem of calculating the electromagnetic fields associated with a dipole located in a semi-infinite conducting medium has been studied continuously for over 60 years. In addition to being mathematically challenging, understanding the fields has considerable practical value.

Once the fields for a given geometry can be calculated (either analytically or numerically), it is easy to compare the relative merits of this form of communication with acoustic and wired systems, in terms of range, power requirements, and bandwidth.

For the geometry shown in Figure 2.1, the electric fields of a dipole antenna can be described in terms of the superposition of plane waves using Fourier integrals. This chapter will outline the basic approach used to arrive at a formulation for the field components with these integrals. The approach is described in great detail by Alfredo Baños in his book "Dipole Radiation in the Presence of a Conducting Half Sphere," and his notation will be used (including $i = \sqrt{-1}$) to facilitate comparison for those interested in filling in the details. Baños treats the cases of vertical and horizontal electric and magnetic dipoles located in the conducting medium (medium 1) and also in the air (medium 2). The following analysis was paraphrased from Baños, omitting material relevant only to the cases involving magnetic sources and sources in the air.

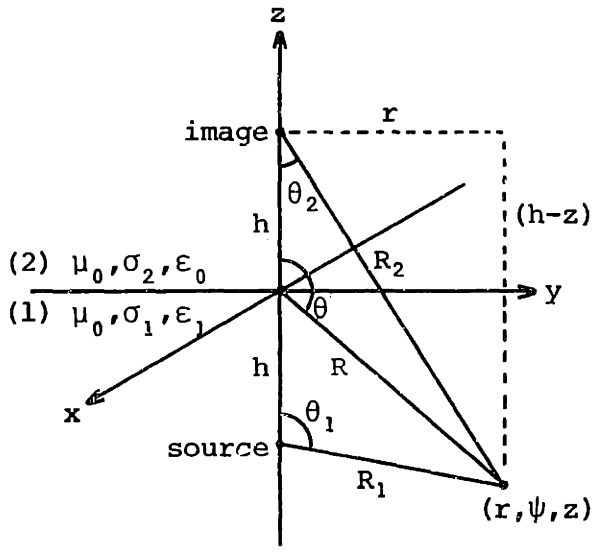

(point of observation shown in y - z plane for clarity)

Mathematical

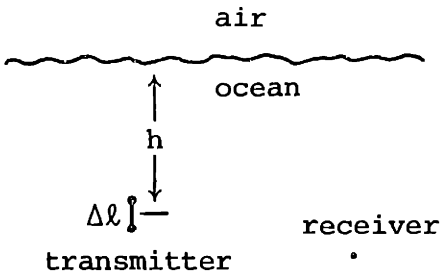

(vertical dipole transmitter shown)

Physical

FIGURE 2.1
BASIC GEOMETRY

It will be assumed that the source consists of a pair of electrodes separated by a distance $\Delta\ell$, connected to a current source of frequency ω and value $I = Ae^{-i\omega t}$, located at a depth h below the surface. For the vertical transmission case, the antenna is aligned with the z-axis, and for the horizontal case, with the x-axis. The receiving antenna consists of a second pair of electrodes, which are used to measure the potential difference produced by the electric field $\vec{E}$ along the length of the antenna. Calculations involving the magnetic field $\vec{H}$ are omitted wherever possible for simplicity. The water is assumed to have conductivity σ_1 mhos/meter, permeability

μ_0 henries/meter, and dielectric constant ε_1 farads/meter. The parameters for air are $\sigma_2 \approx 0$, μ_0, and ε_0.

By using the harmonic time dependence, Maxwell's equations can be written in the form:

$$\begin{aligned} &\text{I.} && \nabla \times \vec{E} - i\omega\mu\vec{H} = 0 \\ &\text{II.} && \nabla \times \vec{H} + i\omega\vec{D} = \sigma\vec{E} \\ &\text{III.} && \nabla \cdot (\mu\vec{H}) = 0 \\ &\text{IV.} && \nabla \cdot \vec{D} = \rho \ . \end{aligned} \qquad [2.1]$$

Using conservation of charge:

$$\nabla \cdot (\sigma\vec{E}) = i\omega\rho \ , \qquad [2.2]$$

and the relationship

$$\vec{D} = \varepsilon\vec{E} + \frac{i}{\omega}\vec{J}^0 \ , \qquad [2.3]$$

where $\vec{J}^0$ is the source current density distribution, Maxwell's equations can be rewritten in the form:

$$\begin{aligned} &\text{I.} && \nabla \times \vec{E} - i\omega\mu\vec{H} = 0 \\ &\text{II.} && \nabla \times \vec{H} + i(\omega\varepsilon + i\sigma)\vec{E} = \vec{J}^0 \\ &\text{III.} && \nabla \cdot \vec{H} = 0 \\ &\text{IV.} && \nabla \cdot (\omega\varepsilon + i\sigma)\vec{E} = -i\vec{J}^0 \ . \end{aligned} \qquad [2.4]$$

The plane wave propagation constant k, and the impedance ζ and admittance η of the medium, are given by:

$$k^2 = \omega^2\mu_0\varepsilon + i\omega\mu_0\sigma \qquad [2.5]$$

$$k\zeta = \omega\mu_0 \text{ , and } k\eta = \omega\varepsilon + i\sigma \text{ .} \qquad [2.6]$$

Substituting [2.5] and [2.6] gives the equations:

$$\begin{aligned} &\text{I.} \quad \nabla \times \vec{E} = ik\zeta\vec{H} \\ &\text{II.} \quad \nabla \times \vec{H} = -ik\eta\vec{E} + \vec{J}^0 \\ &\text{III.} \quad \nabla \cdot \vec{H} = 0 \\ &\text{IV.} \quad \nabla \cdot \vec{E} = \frac{\nabla \cdot \vec{J}^0}{ik} \text{ .} \end{aligned} \qquad [2.7]$$

It can be verified by substitution that [2.7] has the solution:

$$\vec{E} = \nabla\nabla \cdot \vec{\Pi} + k^2\vec{\Pi} \qquad [2.8]$$

where $\vec{\Pi}$ is the electric Hertz vector, or electric polarization potential, if $\vec{\Pi}$ satisfies the inhomogeneous vector Helmholtz equation:

$$(\nabla^2 + k^2)\,\vec{\Pi} = -\frac{i\vec{J}^0}{k\eta} \text{ .} \qquad [2.9]$$

If the distances in the problem are large compared to $\Delta\ell$, the source can be modeled as an elementary electric dipole of moment:

$$p = I\Delta\ell \text{ .} \qquad [2.10]$$

The current density now becomes:

$$\vec{J}^0 = \hat{e}_i\, p\, \delta(x)\, \delta(y)\, \delta(z+h) \qquad (i = 1,2) \text{ ,} \qquad [2.11]$$

$\hat{e}_1 = \hat{e}_x$ for a horizontal dipole, and

$\hat{e}_2 = \hat{e}_z$ for a vertical dipole.

At this point, it becomes convenient to note:

$$k\eta = \frac{k^2}{\omega\mu_0} \text{ ,} \qquad [2.12]$$

which gives:

$$(\nabla^2 + k_1^2)\vec{\Pi}_{1z} = -\left(\frac{ip\omega\mu_0}{k_1^2}\right)\delta(x)\,\delta(y)\,\delta(z+h) \qquad [2.13]$$

and:

$$(\nabla^2 + k_2^2)\vec{\Pi}_{2z} = 0 \qquad [2.14]$$

for a vertical dipole, and:

$$(\nabla^2 + k_1^2)\vec{\Pi}_{1z} = 0\ , \qquad [2.15]$$

$$(\nabla^2 + k_1^2)\vec{\Pi}_{1x} = -\left(\frac{ip\omega\mu_0}{k_1^2}\right)\delta(x)\,\delta(y)\,\delta(z+h)\ , \qquad [2.16]$$

and:

$$(\nabla^2 + k_2^2)\vec{\Pi}_{2z} = (\nabla^2 + k_2^2)\vec{\Pi}_{2x} = 0 \qquad [2.17]$$

for a horizontal dipole.

At the boundary ($z = 0$), the condition that the tangential $\vec{E}$ and $\vec{H}$ fields be continuous gives the relationships:

$$k_1^2\Pi_{1x} = k_2^2\Pi_{2x}\ ,\quad k_1^2\frac{\partial\Pi_{1x}}{\partial z} = k_2^2\frac{\partial\Pi_{2x}}{\partial z}\ ,$$

$$k_1^2\Pi_{1z} = k_2^2\Pi_{2z}\ ,\quad \text{and} \qquad [2.18]$$

$$\frac{\partial\Pi_{1x}}{\partial x} + \frac{\partial\Pi_{1z}}{\partial z} = \frac{\partial\Pi_{2x}}{\partial x} + \frac{\partial\Pi_{2z}}{\partial z}\ .$$

These boundary conditions hold as stated for the horizontal dipole, and give the conditions for the vertical dipole if the x components are set to zero.

At this point, the problem has been reduced to solving the

partial differential equations given in [2.13] through [2.17], subject to the boundary conditions given in [2.18]. For both the vertical dipole and the horizontal dipole, the solution in the water can be split into two parts. The first part corresponds to a particular solution to the inhomogeneous equations [2.13] and [2.16], and the second part corresponds to the solution of the homogeneous equation. For example, the solution to equation [2.13] can be written as:

$$\Pi_{1z} = \Pi_{1z}^{0} + \Pi_{1z}^{1} \quad , \qquad [2.19]$$

where Π_{1z}^{0} is an inhomogeneous solution, and Π_{1z}^{1} is a homogeneous solution.

The particular solution selected by Baños is constructed from the Green's function for the unbounded case:

$$G_{11} = \frac{e^{ik_1 R_1}}{R_1} \quad . \qquad [2.20]$$

It is also convenient at this point to define its image:

$$G_{12} = \frac{e^{ik_1 R_2}}{R_2} \quad , \qquad [2.21]$$

where R_1 and R_2 are defined in Figure 2.1.

G_{11} satisfies the equation:

$$(\nabla^2 + k_1^{\,2}) G_1 = -4\pi\,\delta(x)\,\delta(y)\,\delta(h-z) \quad . \qquad [2.22]$$

This gives (from equation [2.13]):

$$\Pi_{1z}^{0} = \frac{i\omega p \mu_0}{4\pi k_1^{\,2}} G_{11} \quad . \qquad [2.23]$$

The solution for Π_{1x}^{0} for the horizontal dipole is identical, resulting

in:

$$\Pi_{1x}^{0} = \Pi_{1z}^{0} \quad . \tag{2.24}$$

The remaining problem amounts to finding the solution to the homogeneous equation. It is shown in Baños that the Green's function G can be expressed as the superposition of elementary plane waves using the triple Fourier integral:

$$G = \frac{e^{ikR}}{R} = \frac{1}{2\pi^2} \iiint_{-\infty}^{\infty} \frac{e^{i(\xi x + \eta y + \zeta z)}}{\xi^2 + \eta^2 + \zeta^2 - k^2} \, d\xi \, d\eta \, d\zeta \quad . \tag{2.25}$$

By defining the quantity:

$$\gamma = (\xi^2 + \eta^2 - k^2)^{\frac{1}{2}} \xrightarrow[\xi,\eta \to 0]{} -ik \quad , \tag{2.26}$$

and integrating with respect to ζ using residues, G can be expressed as:

$$G = \frac{1}{2\pi} \iint_{-\infty}^{\infty} \frac{1}{\gamma} e^{-\gamma|z| + i(\xi x + \eta y)} \, d\xi \, d\eta \quad . \tag{2.27}$$

If it is assumed that the solutions to the various equations can be expressed in terms of a Fourier integral of the sort used to express G in equation [2.27], then the Hertz vectors of the vertical dipole can be written as:

$$\Pi_{1z} = \frac{i\omega p \mu_0}{4\pi k_1^2} \left\{ G_{11} + \frac{1}{2\pi} \iint_{-\infty}^{\infty} g_1(\xi,\eta) e^{\gamma_1 (z-h) + i(\xi x + \eta y)} d\xi \, d\eta \right\} \tag{2.28}$$

and:

$$\Pi_{2z} = \frac{i\omega p \mu_0}{8\pi^2 k_2^2} \iint_{-\infty}^{\infty} g_2(\xi,\eta) \, e^{-\gamma_1 h - \gamma_2 z + i(\xi x + \eta y)} \, d\xi \, d\eta \quad .$$

By using the boundary conditions in [2.18], and the integral form for G_{12} from [2.27] and [2.21], this can be solved for the appropriate weighting function $g_1(\xi,\eta)$ to get:

$$\Pi_{1z} = \frac{i\omega p \mu_0}{4\pi k_1^2}\left\{G_{11} - G_{12} + k_2^2 \iint_{-\infty}^{\infty} \frac{e^{-\gamma_1(h-z)+i(\xi x+\eta y)}}{k_2^2\gamma_1 + k_1^2\gamma_2}\, d\xi\, d\eta\right\} \qquad [2.29]$$

The integral is axially symmetric, and using the transformations:

$$\begin{aligned} &x = r\cos\psi\ ,\quad y = r\sin\psi\ ,\quad r = (x^2+y^2)^{\frac{1}{2}}\ ,\\ &\xi = \lambda\cos\beta\ ,\quad \eta = \lambda\sin\beta\ ,\quad \text{and } \lambda = (\xi^2+\eta^2)^{\frac{1}{2}}\ , \end{aligned} \qquad [2.30]$$

it can be converted into a single integral in terms of λ:

$$V_{11} \equiv \int_0^{\infty} \frac{2e^{-\gamma_1(h-z)}}{k_2^2\gamma_1 + k_1^2\gamma_2} J_0(\lambda r)\,\lambda\, d\lambda\ , \qquad [2.31]$$

where:

$$\begin{aligned} &\gamma_1 = (\lambda^2 - k_1^2)^{\frac{1}{2}} \xrightarrow[\lambda\to 0]{} -ik_1\ ,\ \text{and}\\ &\gamma_2 = (\lambda^2 - k_2^2)^{\frac{1}{2}} \xrightarrow[\lambda\to 0]{} -ik_2\ , \end{aligned} \qquad [2.32]$$

to ensure convergence of the integral by guaranteeing only decaying exponentials with $R_e(\gamma_1,\gamma_2) > 0$, and J_0 is a Bessel function of order zero.

The two terms γ_1 and γ_2 contribute four branch points to the integrand. γ_1 has two branch points at plus and minus k_1, and γ_2 has branch points at plus and minus k_2 (see Figure 2.2).

This completes the derivation of the expression for Π_{1z}, which

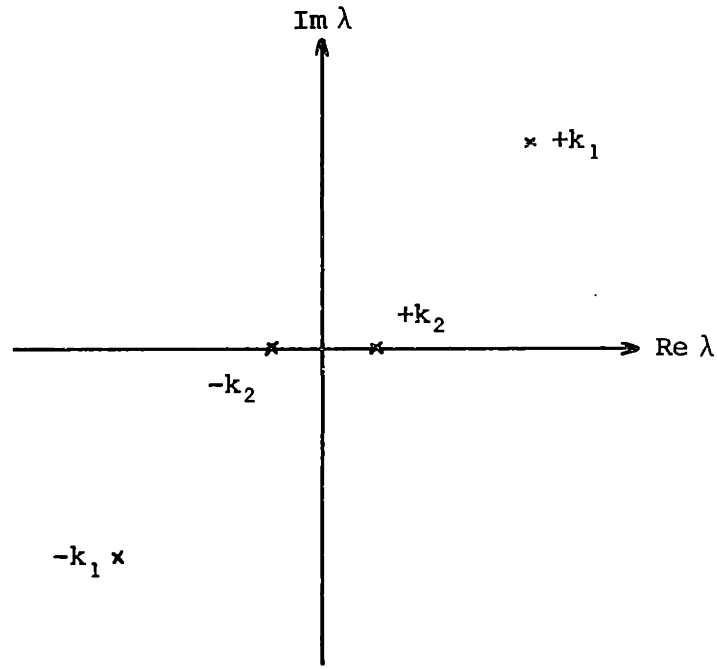

FIGURE 2.2
SINGULARITIES IN THE COMPLEX λ PLANE

can now be written in the final form:

$$\Pi_{1z} = \frac{i\omega p\mu_0}{4\pi k_1^2} \left\{ G_{11} - G_{12} + k_2^2 V_{11} \right\} . \qquad [2.33]$$

For the horizontal dipole, a similar analysis can be followed, yielding (for the x component):

$$\Pi_{1x} = \frac{i\omega p\mu_0}{4\pi k_1^2} \left\{ G_{11} - G_{12} + U_{11} \right\} . \qquad [2.34]$$

where:

$$U_{11} = \int_0^\infty \frac{2e^{-\gamma_1 (h - z)} J_0(\lambda r)\, \lambda\, d\lambda}{\gamma_1 + \gamma_2} . \qquad [2.35]$$

The solution for the z component is slightly different, but follows along the same general lines. First, the solution is assumed to be of the form:

$$\Pi_{1z} = \frac{i\omega p\mu_0}{8\pi^2 k_1^2} \iint_{-\infty}^{\infty} i\xi\, g_1(\xi,\eta)\, e^{\gamma_1(z-h) + i(\xi x + \eta y)}\, d\xi\, d\eta \ ,$$

and: [2.36]

$$\Pi_{2z} = \frac{i\omega p\mu_0}{8\pi^2 k_2^2} \iint_{-\infty}^{\infty} i\xi\, g_2(\xi,\eta)\, e^{-\gamma_1 h - \gamma_2 z + i(\xi x + \eta y)}\, d\xi\, d\eta \ .$$

The term $i\xi$ has been included explicitly for convenience, and can be made implicit by taking the partial derivative of the rest of the integrand with respect to x. Using this and the boundary conditions in [2.18], Π_{1z} can be written:

$$\Pi_{1z} = \frac{i\omega p\mu_0}{4\pi k_1^2} \frac{\partial W_{11}}{\partial x} \ , \qquad [2.37]$$

where:

$$W_{11} = \frac{1}{2\pi} \iint_{-\infty}^{\infty} \frac{2(\gamma_2 - \gamma_1) e^{-\gamma_1(h-z) + i(\xi x + \eta y)}}{k_2^2 \gamma_1 + k_1^2 \gamma_2}\, d\xi\, d\eta \ . \qquad [2.38]$$

By using [2.27], [2.29], and [2.30], W_{11} can be expressed in terms of previously defined quantities:

$$W_{11} = \frac{\partial}{\partial z}\left(2G_{12} - (k_1^2 + k_2^2)V_{11}\right) \ . \qquad [2.39]$$

The actual field components can now be expressed in terms of the four functions G_{11}, G_{12}, V_{11}, and U_{11} with the application of [2.8]. The three components of the electric field for a vertical dipole are:

$$E_{1r} = \frac{i\omega p\mu_0}{4\pi k_1^2}\left\{\frac{\partial^2}{\partial r\, \partial z}\left(G_{11} - G_{12} + k_2^2 V_{11}\right)\right\} \ ,$$

$$E_{1\psi} = 0 \ , \text{ and} \qquad [2.40]$$

$$E_{1z} = \frac{i\omega p\mu_0}{4\pi k_1^2}\left\{\left(\frac{\partial^2}{\partial z^2} + k_1^2\right)\left(G_{11} - G_{12} + k_2^2 V_{11}\right)\right\} \ .$$

The fields for a horizontal dipole are:

$$E_{1r} = \frac{i\omega p\mu_0}{4\pi k_1^2} \cos\psi \left\{ \frac{\partial^2}{\partial r^2} (G_{11}-G_{12}+k_1^2 V_{11}) + k_1^2 (G_{11}-G_{12}+U_{11}) \right\} ,$$

$$E_{1\psi} = -\frac{i\omega p\mu_0}{4\pi k_1^2} \sin\psi \left\{ \frac{1}{r} \frac{\partial}{\partial r} (G_{11}-G_{12}+k_1^2 V_{11}) + k_1^2 (G_{11}-G_{12}+U_{11}) \right\} , \quad [2.41]$$

and:

$$E_{1z} = \frac{i\omega p\mu_0}{4\pi k_1^2} \cos\psi \left\{ \frac{\partial^2}{\partial z\, \partial r} (G_{11}-G_{12}-k_1^2 V_{11}) \right\} .$$

Because of the nature of the two complex integrals V_{11} and U_{11}, no simple analytic solution to these equations exists for the general case. In Baños, extensive use of saddle point integration techniques is made to provide approximate solutions to the integrals for limited cases. In the following chapter (Chapter 3), a numerical integration computer program is described which was developed to evaluate V_{11} for use in the vertical antenna problem, and Chapter 7 includes an exact evaluation of U_{11} for the case of a horizontal dipole at the surface.

The electric fields of both a vertical and a horizontal submerged antenna have been formulated in terms of the infinite medium Green's function and its image (both in the form of spherical waves), and in terms of two complex integrals. The Green's function corresponds to a particular solution to the inhomogeneous vector Helmholtz equation governing the problem. The homogeneous solution (consisting of the image term and the integral terms) was derived by matching boundary conditions for the various components of the vector potential by assuming the solution could be written as a superposition of plane waves in the form of a Fourier integral. After matching the

boundary conditions, the Fourier integrals were then split into the sum of image and integral terms from which the components of the electric fields could then be computed. Although the complex integrals cannot be analytically evaluated for the general case, saddle point method solutions can be calculated for some special cases, and numerical solutions can be computed to allow comparison with experimental results and to facilitate the evaluation and design of possible communications systems.

CHAPTER 3

THE VERTICAL TRANSMISSION CASE AND COMPUTER ANALYSIS

The case of vertical transmission in the ocean, either from a submerged instrument to the surface or vice versa, is one of great practical importance. A method of predicting the field behavior for this case would be very useful for determining the value of such a communications system.

In his book, Baños spends considerable effort on the computation of the fields near the vicinity of the vertical axis using the method of steepest descents, or saddle point method, to evaluate the complex integrals involved in the field equations. This technique requires the term-by-term integration of a function involving a powers series. The power series expansion has a finite radius of convergence dependent upon the particular function being integrated and its parameters. (For a discussion of this technique, see Baños Chapter 3.)

Unfortunately, for the field integrals near the vertical axis, and the physical parameters and frequencies of interest, the series converges very slowly and is therefore of little practical value for finding the fields in the ocean (see Baños Section 5.3). For this reason, numerical techniques were used to evaluate the integral involved in the vertical field calculations.

Because the field of a static dipole is strongest in the axial direction, it was decided to analyze the case of vertical transmission

from a vertical dipole. Using the approach outlined in the preceding chapter, the following expression can be derived for the z component of the electric field of a vertical electric dipole (using the geometry of Figure 2.1):

$$E_z = \frac{i\omega p \mu_0}{4\pi k_1^2} \left\{ \left(\frac{\partial^2}{\partial z^2} + k_1^2 \right) (G_{11} - G_{12} + k_2^2 V_{11}) \right\} , \qquad [3.1]$$

where:

$i = \sqrt{-1}$ (to be consistent with Banos),

p is the dipole moment of the source (assuming an $e^{-i\omega t}$ time dependence),

μ_0 is the permeability of the water (assumed to be equal to that of air),

k_1 and k_2 are the homogeneous plane wave propagation constants for sea water and air respectively,

$$G_{11} = \frac{e^{ik_1 R_1}}{R_1} , \qquad [3.2]$$

$$G_{12} = \frac{e^{ik_1 R_2}}{R_2} , \qquad [3.3]$$

$$V_{11} = \int_0^\infty \frac{2\lambda e^{-\gamma_1 (h-z)} J_0(\lambda_r)\, d\lambda}{k_2^2 \gamma_1 + k_1^2 \gamma_2} , \qquad [3.4]$$

$$\gamma_m = (\lambda^2 - k_m^2)^{\frac{1}{2}} \quad (\text{for } m = 1,2), \qquad [3.5]$$

R_1, R_2, r, h, and z are as defined in Figure 2.1, and

$J_0(\lambda_r)$ is a Bessel function of order zero.

The term G_{11} corresponds to the Green's function for the unbounded conducting medium, and has the form of an elementary spherical wave. G_{12} is the image function of G_{11}. This image term and the V_{11} term form the solution to the homogeneous Helmholtz equation. The three terms form the complete solution to the inhomogeneous Helmholtz equation governing the problem (G_{11} being a particular solution to the inhomogeneous equation). It is the evaluation of the V_{11} integral which is the primary difficulty in finding E_z.

Before the analysis was begun, a number of simplifying assumptions were made. First, if the analysis is restricted to examining only the field in a direct vertical line with the source, then $r = 0$, the Bessel function takes on the value 1, and it can be removed from the integral. From Figure 2.1, this also allows R_1 and R_2 to be expressed only in terms of h and z:

$$R_1 = h + Z \text{ , and}$$
$$R_2 = h - z \text{ .} \qquad [3.6]$$

Next, by examining the propagation constants:

$$k_1^2 = \omega^2 \mu_0 \varepsilon_1 + i\omega\mu_0\sigma_1 \text{ , and} \qquad [3.7]$$

$$k_2^2 = \omega^2 \mu_0 \varepsilon_0 + i\omega\mu_0 \text{ ,} \qquad [3.8]$$

where:

μ_0 is the permeability in henries/meter for both media,

ε_1 and ε_0 are the dielectric constants in farads/meter for sea water and air respectively, and

σ_1 and σ_2 are the conductivity in mhos/meter of sea water and air respectively,

it can be shown that (for the frequencies of interest):

$$k_1^2 \approx i\omega\mu_0\sigma_1 \equiv iT \text{ , and} \qquad [3.9]$$

$$k_2^2 \approx \omega^2\mu_0\varepsilon_0 \equiv A \text{ .} \qquad [3.10]$$

For mathematical reasons, it is necessary to assume that k_2^2 has a small but finite imaginary part, but this has no effect on the actual calculations.

The last assumption made was that the dipole strength (equal to the antenna current times its length) is unity. This simplifies the calculations, and because the field is linearly proportion to p, the results are easily scaled for other values of p.

Equation [3.1] can now be split into two parts, one corresponding to the Green's functions, and one corresponding to the integral. E_z can be expressed (using [3.9] and [3.10]) as the sum of E_{z1} and E_{z2} given by:

$$E_{z1} = \frac{1}{4\pi\sigma_1}\left\{\left(\frac{\partial^2}{\partial z^2} + iT\right)(G_{11} - G_{12})\right\} \text{ , and} \qquad [3.11]$$

$$E_{z2} = \frac{A}{4\pi\sigma_1}\left\{\left(\frac{\partial^2}{\partial z^2} + iT\right)V_{11}\right\} \text{ .} \qquad [3.12]$$

V_{11} can now be written (using A and T) as:

$$V_{11} = \int_0^\infty \frac{2\lambda e^{-(\lambda^2 - iT)^{\frac{1}{2}}(h-z)}\, d\lambda}{A(\lambda^2 - iT)^{\frac{1}{2}} + iT(\lambda^2 - A)^{\frac{1}{2}}} \quad . \qquad [3.13]$$

Taking the partial derivatives with respect to z gives:

$$E_{z1} = \frac{1}{2\pi\sigma_1}\left(ik_1 \left(-\frac{e^{ik_1R_1}}{R_1^2} + \frac{e^{ik_1R_2}}{R_2^2} \right) + \left(\frac{e^{ik_1R_1}}{R_1^3} - \frac{e^{ik_1R_2}}{R_2^3} \right) \right) , \text{ and} \qquad [3.14]$$

$$E_{z2} = \frac{A}{2\pi\sigma_1} \int_0^\infty \frac{\lambda^3 e^{-(\lambda^2 - iT)^{\frac{1}{2}}(h-z)}\, d\lambda}{A(\lambda^2 - iT)^{\frac{1}{2}} + iT(\lambda^2 - A)^{\frac{1}{2}}} \quad . \qquad [3.15]$$

By taking the positive root of k_1^2 in equation [3.9] (to avoid growing exponential solutions), k_1 is given by:

$$k_1 = (iT)^{\frac{1}{2}} = \left(\frac{T}{2}\right)^{\frac{1}{2}} + i\left(\frac{T}{2}\right)^{\frac{1}{2}} \quad . \qquad [3.16]$$

Using this, the evaluation of E_{z1} is a relatively straightforward problem.

Now, attention can be directed to the evaluation of the integral in equation [3.15]. Before proceeding with the integration, the exact nature of the integrand must be examined with regard to its singularities in the complex λ plane.

First, in order to ensure exponentially decaying values in the integrand of equation [3.15] (and similar equations for other field components involving $e^{-\gamma_2}$), it is necessary to require:

$$\gamma_1 = (\lambda^2 - iT)^{\frac{1}{2}} \xrightarrow[\lambda \to 0]{} -i\,(iT)^{\frac{1}{2}} \text{ , and} \qquad [3.17]$$

$$\gamma_2 = (\lambda^2 - A)^{\frac{1}{2}} \xrightarrow[\lambda \to 0]{} - i\,(A)^{\frac{1}{2}} \,. \qquad [3.18]$$

This guarantees the Re $\{\gamma_1, \gamma_2\} > 0$ for λ on the real λ axis. Next, a cut λ plane must be chosen in which the integrand is a single valued analytic function of λ. The integrand has branch points at $\pm k_1$ from γ_1, and $\pm k_2$ from γ_2 as shown in Figure 3.1. The branch cuts are taken from the branch points to infinity along paths which do not cross the real λ axis (the path of integration). In addition, it must be assumed (as was mentioned earlier) that k_2^2 has a small positive imaginary part to force it off the real axis and to avoid the mathematically questionable process of integrating through a branch point. For the parameters of interest, the real and imaginary parts

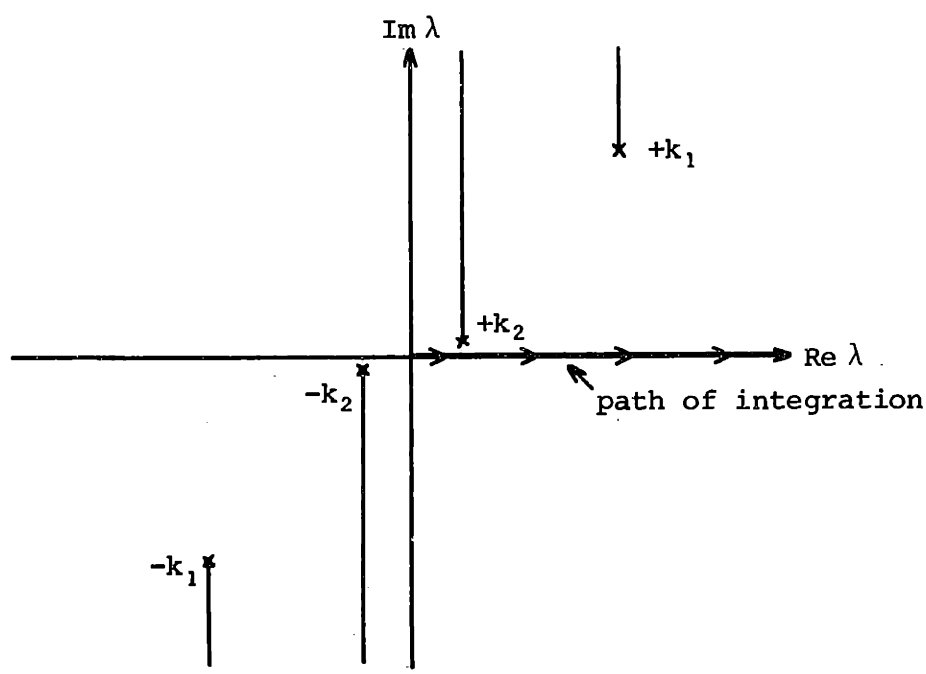

FIGURE 3.1
SINGULARITIES AND BRANCH CUTS IN THE COMPLEX λ PLANE

of the γ_1 term in the denominator of [3.15] are always much larger than the contribution to the denominator from a small imaginary part added to $k_1^2 = A$, and the effect of this assumption is completely negligible in the calculation of the integral.

It is possible, depending on how γ_1 and γ_2 are evaluated, for the denominator of the integrand to go to zero, thus forming a pole. However, this pole only exists on two of the four Riemann sheets of the complex λ plane. In effect, if the roots of γ_1 and γ_2 are evaluated to give the same sign for the two terms (either plus or minus), they will add, and the integrand will not go to zero. If the signs of the two terms are opposite, then they will cancel to zero for some values of λ, creating a pole in the integrand. Because of the selection in signs in equations [3.17] and [3.18], this pole will not be present on the Riemann sheet of interest. (For a detailed discussion of this problem, see Baños, Section 2.64.)

The integrand is now a well-defined single-valued function along the path of integration, and the problem of numerically integrating the function remains.

The APL computer language was selected, primarily for reasons of availability and familiarity. APL also has the advantage that complex numbers can be easily manipulated in the form of two-element vectors using the extensive library of primitive vector functions available in the language.

The first step in evaluating the field was the implementation of a routine to generate values of the integrand (separated into its real and imaginary parts) for any given values of frequency (F),

transmitter depth (TD), receiver depth (RD), conductivity (C), and integration variable (L). The implementation of this routine (called FUNC) is described in detail in the appendix.

Before the integral was computed, the behavior of the integrand for various values of F, L, and TD was examined to determine how to perform the integration in as simple and efficient a manner as possible. The behavior of the real part of the integrand for C = 4 mhos/m, F = 100 kHz, RD = 1, and TD = 7 is shown in Figure 3.2, and the behavior for TD = 3 is shown in Figure 3.3.

On the scale of the graphs in Figures 3.2 and 3.3, the integrand appears to be a smooth function which converges rapidly to zero for values of L greater than 4 or 5. However, examination of the behavior of the integrand in the vicinity of $L = \sqrt{A}$, where γ_2 changes from a complex to a real number (shown in Figure 3.4 for the same parameters as Figure 3.2), shows a dramatic "doublet." Fortunately, for the range of frequencies being considered, the size of this doublet is almost undetectable on the scale of the rest of the integrand, and its overall contribution to the integral will be quite insignificant, considering its overall height and width.

Because the integrand is a fairly smooth function (ignoring the doublet at $\sqrt{A}$), a simple constant step-size trapezoidal integration algorithm was selected to perform the numerical integration. After examining the behavior of the real and imaginary parts of the integrand for various parameter values over the range of interest, two empirical formulas were developed to calculate an appropriate step-size (H) and upper integration limit (LM) as a function of T and R_2.

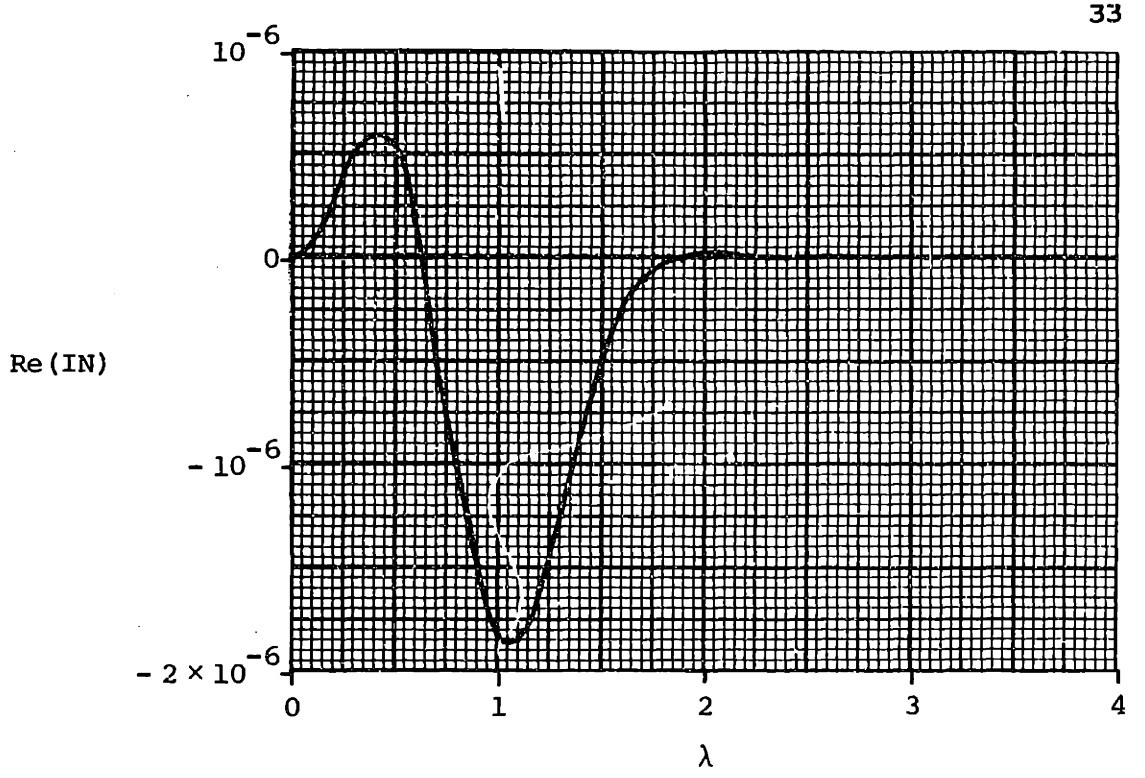

FIGURE 3.2
Re(IN) PLOTTED FOR TD = 7

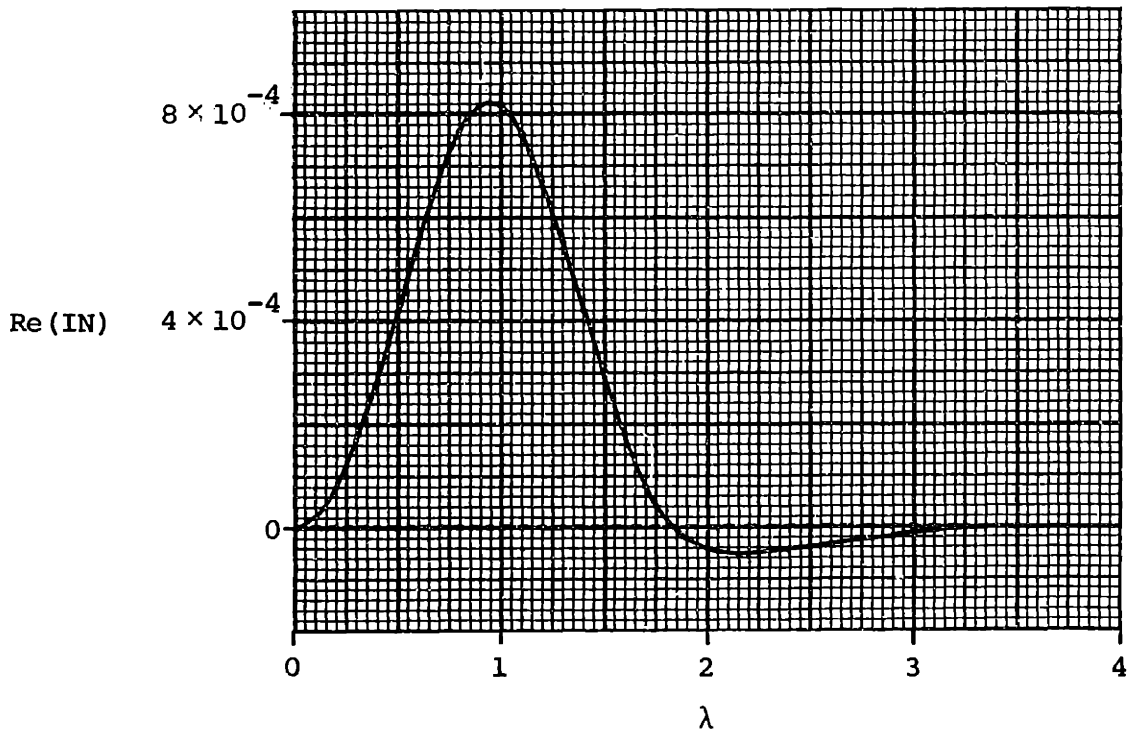

FIGURE 3.3
Re(IN) PLOTTED FOR TD = 3

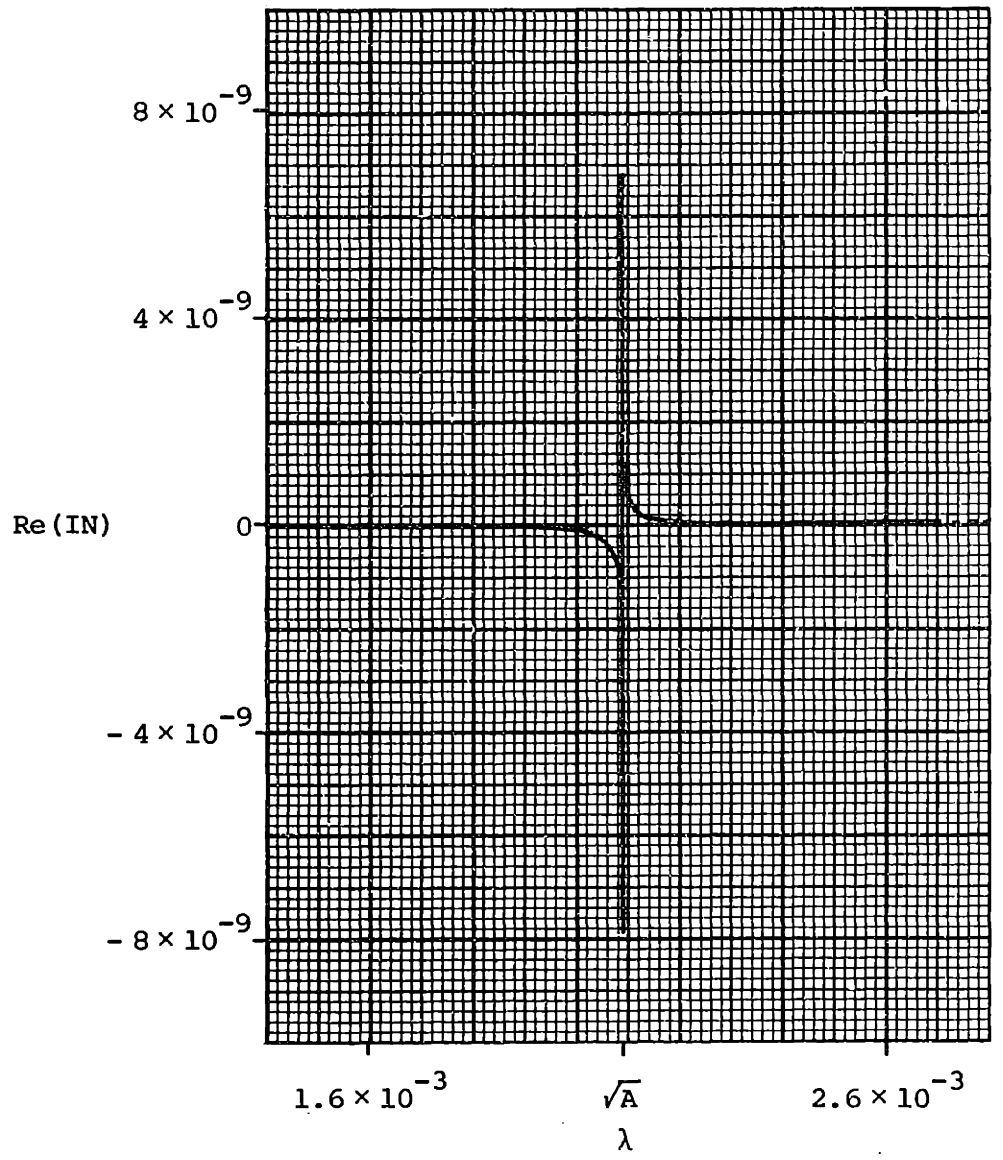

FIGURE 3.4
BEHAVIOR OF Re(IN) IN THE VICINITY OF $\sqrt{A}$

These formulas were chosen to be as conservative as possible without unnecessary iterations, and are given below:

$$H = .005 + .025 \times \sqrt{T} \text{ , and} \qquad [3.19]$$

$$LM = 1 + 12 \times \frac{\sqrt{T}}{R_2} \text{ .}$$

The operation of the final program (called VFIELD) is described in the appendix.

This program was used to evaluate the attenuation of a signal with depth for comparison with experimental results, and it was also used to calculate the frequency dependence of the received signal for use in the noise analysis. After calculating the field strength for a variety of parameters, and comparing the results with the magnitude of E_{z_1} for each case, it was found that the only appreciable contribution to the actual field comes from the two Green's function terms, and not from the integral term. The complete program was used to evaluate the fields discussed later, but neglecting the integral term in future work will produce identical results (to three or four decimal places) over the frequencies and ranges treated here. The only case where the integral becomes important is when the source is sufficiently close to the surface that the source and image Green's functions are close to cancelling each other. With the source placed at the depths used in the experimental tests, this is not a problem. Although it could become important for the case of transmission from the surface down to a submerged receiver, this case can easily be treated by using reciprocity.

CHAPTER 4

VERTICAL FIELD MEASUREMENTS

In order to provide experimental verification of the computer analysis of the vertical field covered in the preceding chapter, a 100 kHz transmitter and receiver were constructed, and measurements were taken of the attenuation of the field as the transmitter was lowered into the water. 100 kHz was selected as the operating frequency to obtain a sufficiently fast decay that reflected signals from the bottom and any nearby structures could be ignored. The receiving antenna was located above the transmitter to avoid passing the receiving antenna cable directly past the transmitter on its way to the surface.

The actual tests were done in the large "well" in the Woods Hole Oceanographic Institution dock area. This is an open space approximately 4 meters wide and 10 meters long over water about 15 meters deep. The nearest support pilings were at least 4 or 5 meters away from the receiver location.

A diagram of the arrangement of the equipment is shown in Figure 4.1. The antenna electrodes were made of 1.5 inch long sections of 1.5 inch diameter copper pipe, which were fastened with plastic bolts to sections of acrylic rod. A styrofoam float was used to support the weight of the transmitter and a 4 pound lead ballast weight, in addition to holding the receiving antenna at a fixed depth. The line (with depth markings) was passed through all four antenna electrodes

to hold the antennas in a coaxial orientation. The receiving equipment was located in a nearby wooden rowboat.

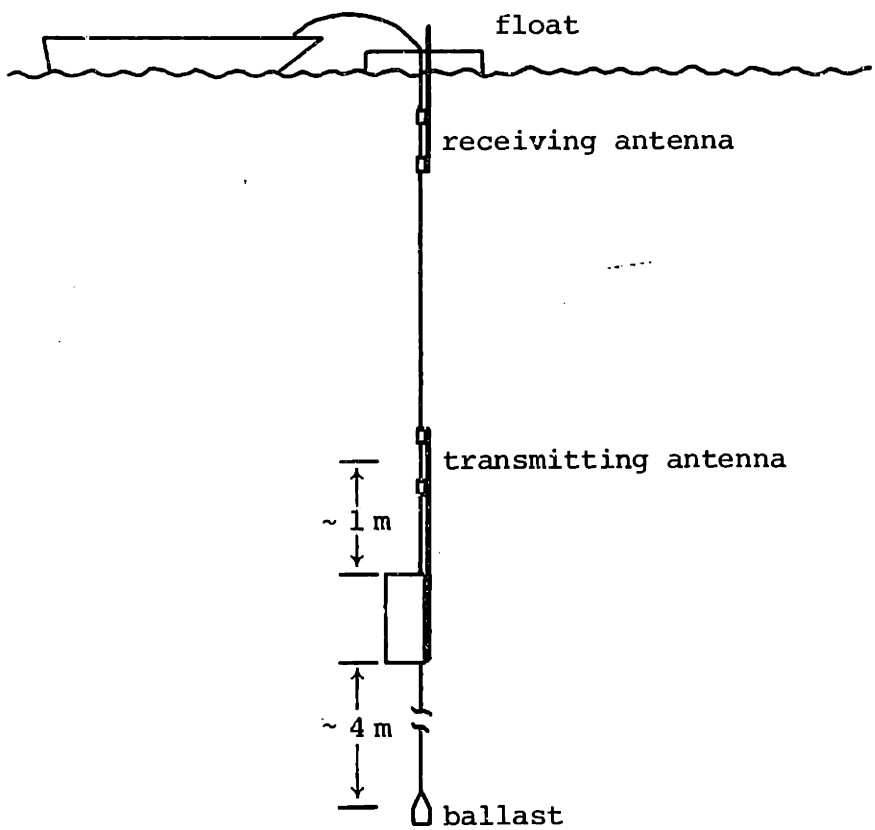

FIGURE 4.1
VERTICAL FIELD EXPERIMENTAL SETUP

The antenna's impedance was roughly two ohms at 100 kHz. In order to eliminate problems resulting from variations in this impedance, the receiver was designed to have a very high input resistance, and the transmitter was constructed to operate as a current source.

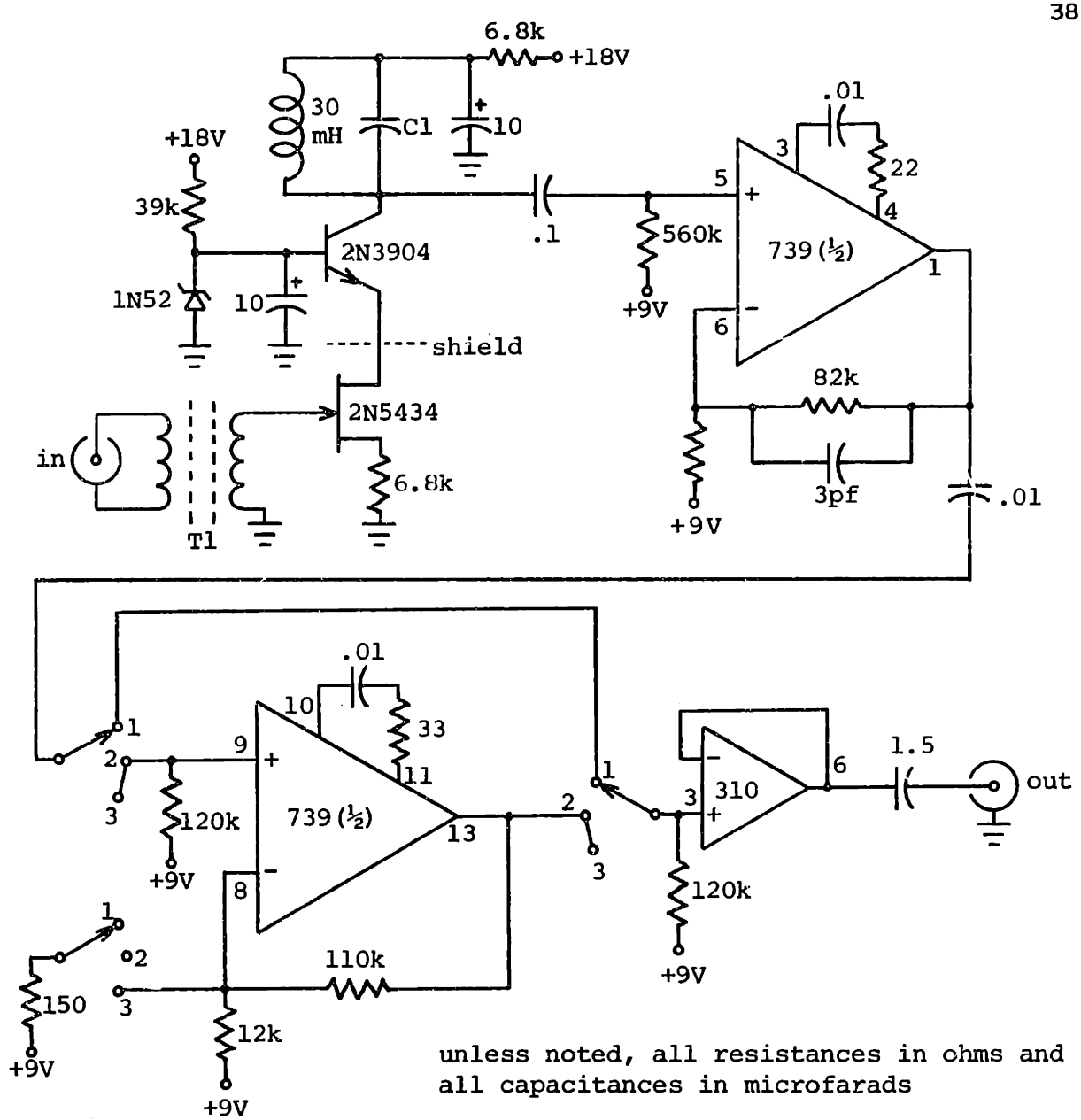

unless noted, all resistances in ohms and all capacitances in microfarads

T1 = 4 turns #20:400 turns #34, C1 = 54 pf for 100 kHz

T1 = 9 turns #20:900 turns #34, C1 = .0086 f for 10 kHz

Ferroxcube 2616 core, 3B9 ferrite

FIGURE 4.2
TUNED PREAMPLIFIER SCHEMATIC

The "receiver" consisted of a tuned pre-amplifier and a portable oscilloscope. A schematic of the pre-amp is shown in Figure 4.2. The input stage consists of a 1:100 transformer driving an F.E.T. cascode stage with a tuned load. This stage has a bandwidth of about 7 kHz to cut down out-of-band noise. Including the transformer, this input section has a gain of roughly 5,000. The next stage provides a gain of 2 to give an overall gain of 10,000 at the lowest switch setting. The next stage has a selectable gain of either 10 or 100, followed by an output buffer. Power was provided by two 9 volt "transistor" batteries. In order to prevent the input from saturating on out-of-band transients, the cascode was operated from the full 18 volt supply, which necessitated the unorthodox grounding arrangement. A photograph of the preamplifier is shown in Figure 4.3.

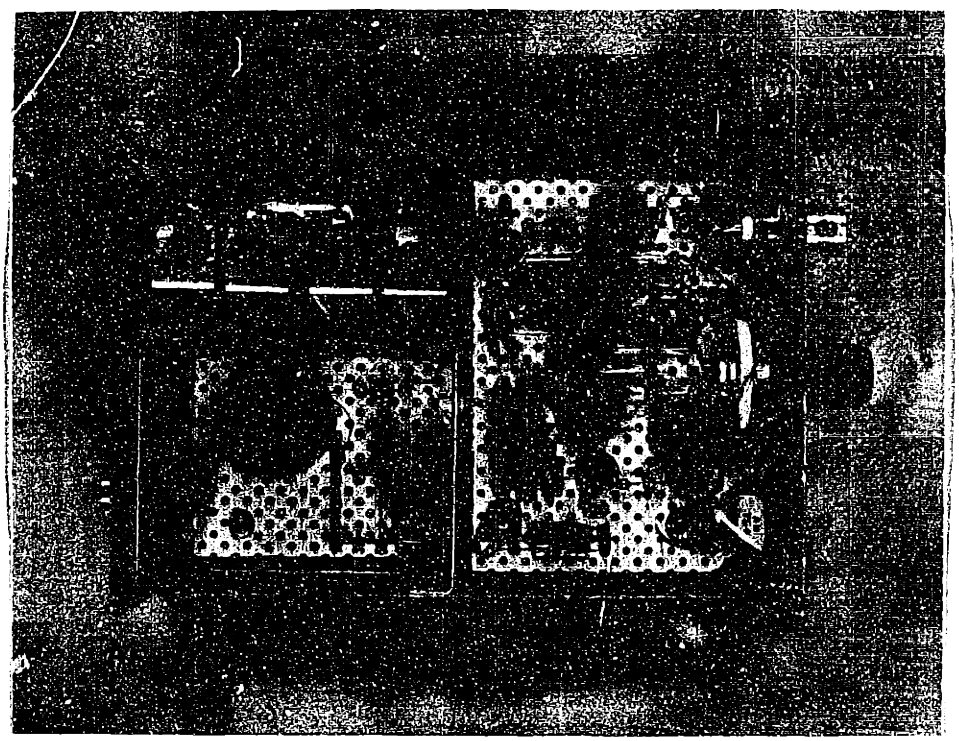

FIGURE 4.3
TUNED PREAMPLIFIER
(shielded enclosure for input section on left)

The "receiver" consisted of a tuned pre-amplifier and a portable oscilloscope. A schematic of the pre-amp is shown in Figure 4.2. The input stage consists of a 1:100 transformer driving an F.E.T. cascode stage with a tuned load. This stage has a bandwidth of about 7 kHz to cut down out-of-band noise. Including the transformer, this input section has a gain of roughly 5,000. The next stage provides a gain of 2 to give an overall gain of 10,000 at the lowest switch setting. The next stage has a selectable gain of either 10 or 100, followed by an output buffer. Power was provided by two 9 volt "transistor" batteries. In order to prevent the input from saturating on out-of-band transients, the cascode was operated from the full 18 volt supply, which necessitated the unorthodox grounding arrangement. A photograph of the preamplifier is shown in Figure 4.3.

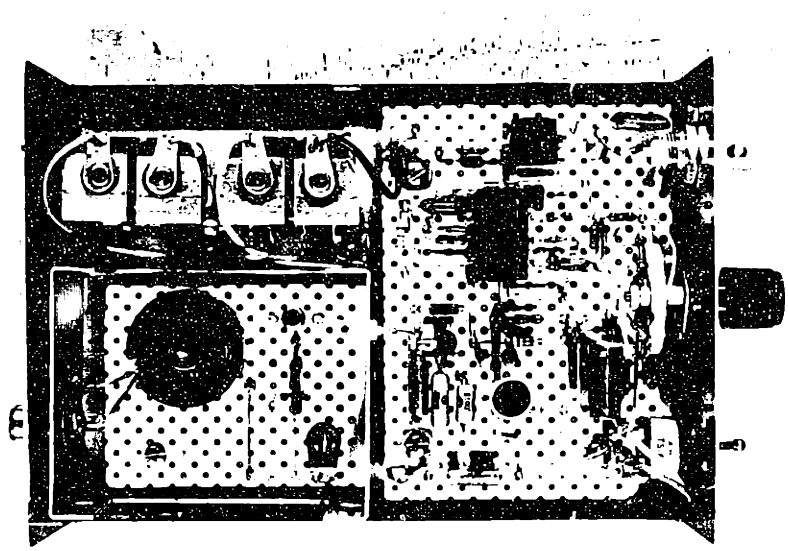

FIGURE 4.3
TUNED PREAMPLIFIER
(shielded enclosure for input section on left)

The schematic for the transmitter is shown in Figure 4.4. The upper part of the circuit consists of a C.M.O.S. astable multivibrator and a Colpitts oscillator. The oscillator operates at 100 kHz, and is gated on and off at five second intervals by the astable. This allows easy comparison of the signal and noise levels. The power amplifier is a one ampere r.m.s. feedback current source circuit using the .4 Ω resistor for the current sense. The LM318 operational amplifier was chosen for its high frequency performance, which is required to obtain a reasonable loop transmission at 100 kHz and still provide enough voltage gain to avoid wasting power in the current sense resistor. The power output stage is a complementary push-pull arrangement, with relatively small crossover distortion. The driver circuit was originally designed for much higher gain transistors than those indicated, but they could not be obtained in time for the experiments. As a result, considerable extra power was dissipated in the bias resistors. This could be corrected by replacing the output transistors with a complementary Darlington connection, but heat sink space was too limited to make this modification. The two diodes on the output and the 1.5 kΩ resistor on the inverting input of the LM318 are designed to prevent transient damage when the current source is open circuited. Power was supplied by two packs of six Gates sealed rechargeable lead-acid D-cells. A photograph of the transmitter circuit is shown in Figure 4.5.

The housing for the transmitter was constructed out of a 15 inch length of 4 inch schedule 80 P.V.C. pipe. The end cap supporting most of the circuitry had a $\frac{1}{2}$ inch thick aluminum disk mounted on it to

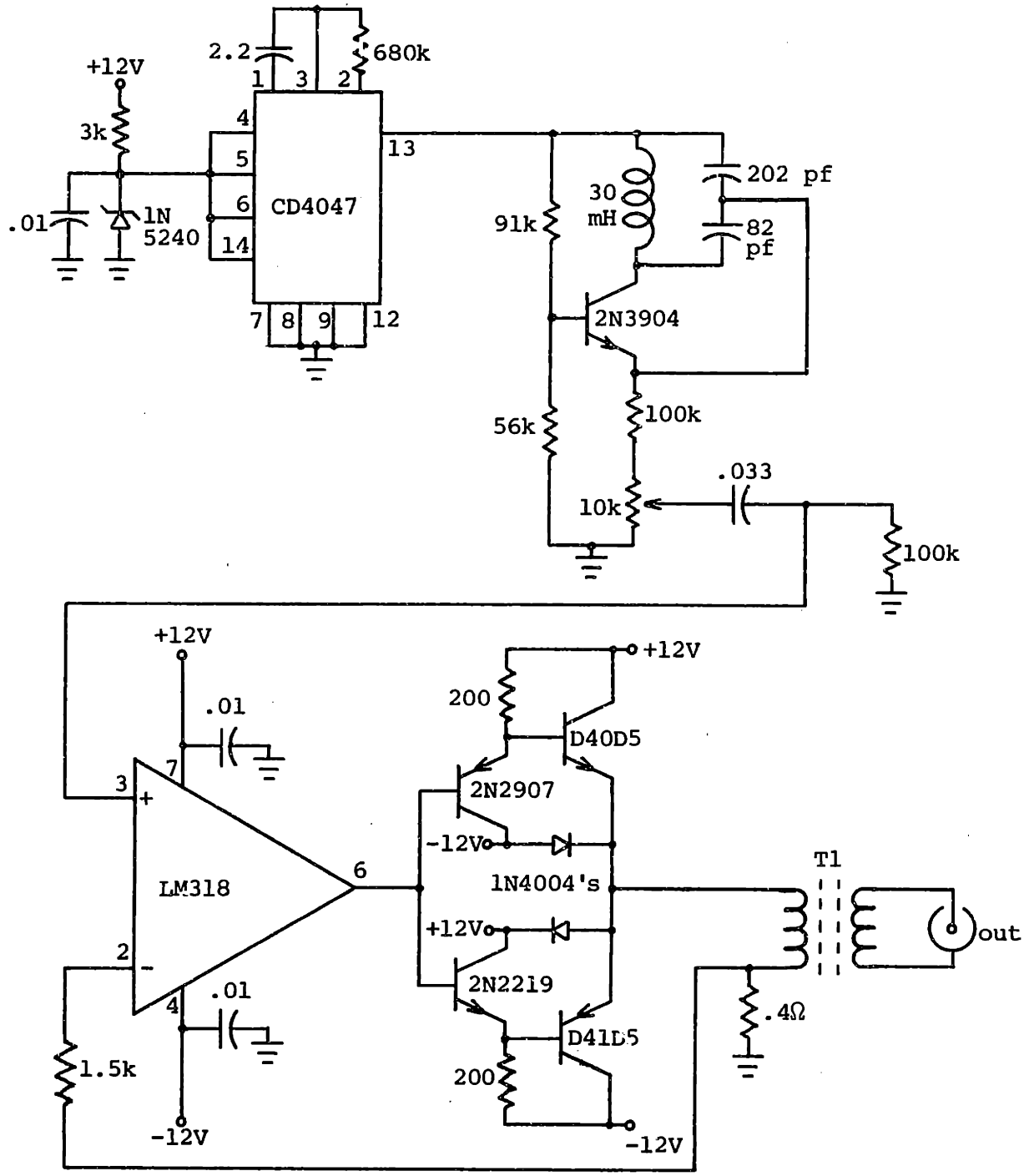

T1 = 8 turns #18:4 turns #16
Ferroxcube 2616P core, 3B9 ferrite

FIGURE 4.4
100 KHZ TRANSMITTER SCHEMATIC

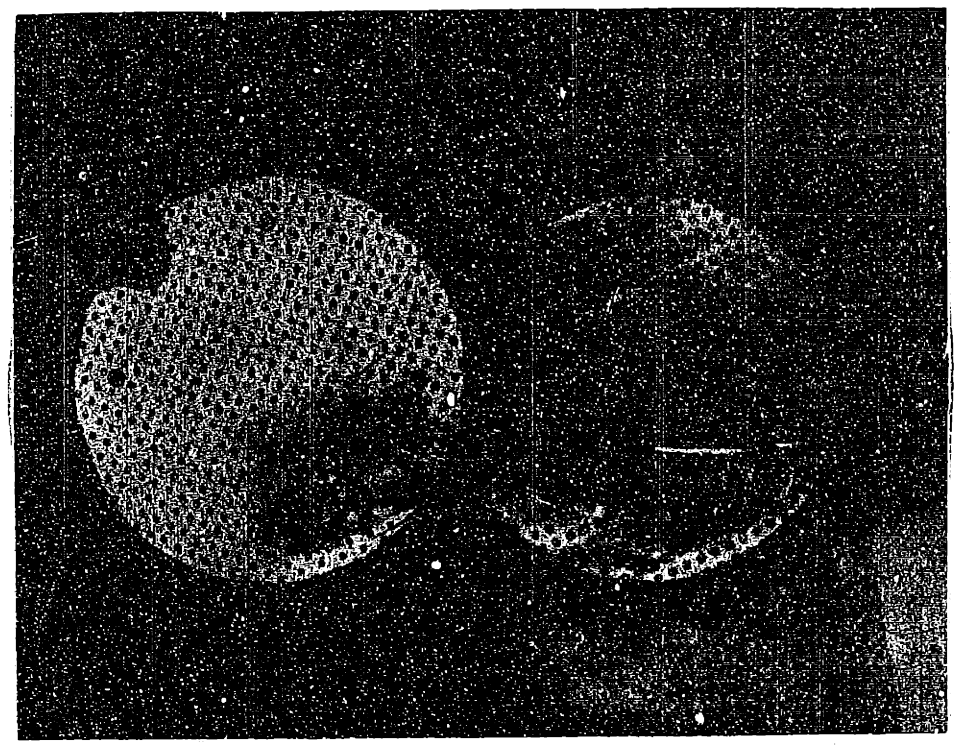

FIGURE 4.5
100 KHZ 1A TRANSMITTER CIRCUITRY
(power transistors mounted underneath main board)

serve as a heatsink. All four of the power transistors were fastened on the inside of the heatsink through a hole in the end cap. The end caps and heatsink were all sealed with O-rings. The other end cap held the output transformer, the power switch, and the output connector. The output switch was sealed with a silicone rubber toggle-switch boot. The output connector was made with a female phono jack epoxied into the end cap, and mated to a phono plug potted onto the cable. The connection was sealed with a short piece of flexible tubing clamped over the two connectors. The entire housing was pressure tested at 4 atmospheres for one hour with no sign of leakage. A photograph of the housing assembly is shown in Figure 4.6.

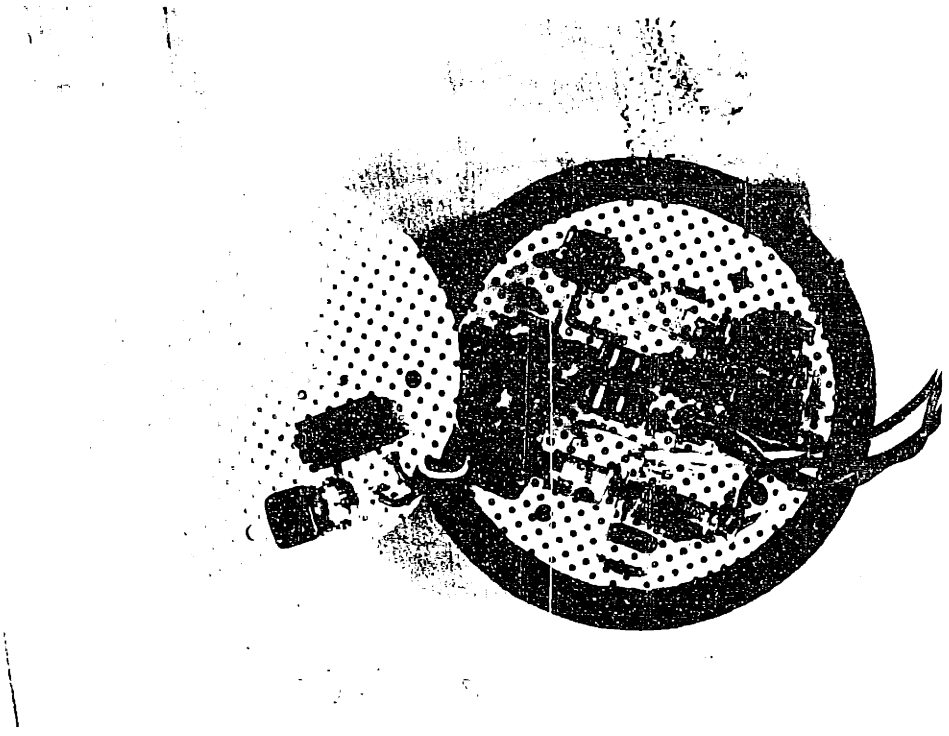

FIGURE 4.5
100 KHZ 1A TRANSMITTER CIRCUITRY
(power transistors mounted underneath main board)

serve as a heatsink. All four of the power transistors were fastened on the inside of the heatsink through a hole in the end cap. The end caps and heatsink were all sealed with O-rings. The other end cap held the output transformer, the power switch, and the output connector. The output switch was sealed with a silicone rubber toggle-switch boot. The output connector was made with a female phono jack epoxied into the end cap, and mated to a phono plug potted onto the cable. The connection was sealed with a short piece of flexible tubing clamped over the two connectors. The entire housing was pressure tested at 4 atmospheres for one hour with no sign of leakage. A photograph of the housing assembly is shown in Figure 4.6.

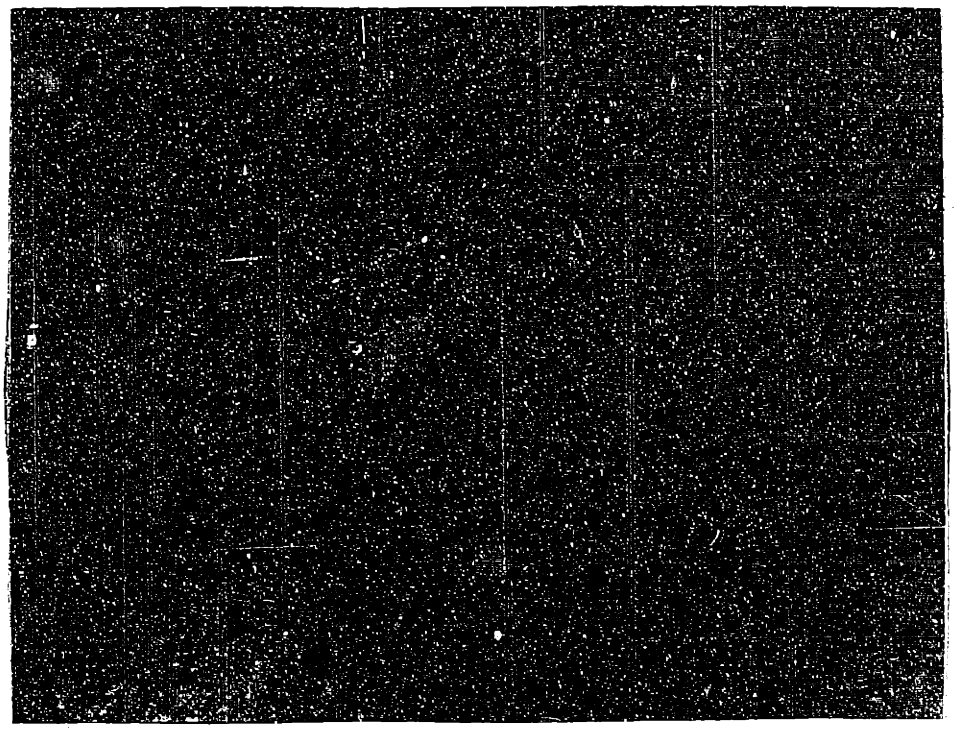

FIGURE 4.6
TRANSMITTER HOUSING

The first series of measurements was taken with the receiving antenna 1 meter below the surface. The field was measured first as the transmitter was lowered into the water, and then again as it was raised. Figure 4.7 shows a plot of the experimental data, and theoretical curves for conductivities of 4.2 mhos/m and 3.57 mhos/m. From the water temperature on the day of the experiment, and the water density on the previous day (density for the day of the experiment was not available, but the two should be quite close), the conductivity was calculated[14,15] to be approximately 4.2 mhos/m. From the plot, it is clear that 3.57 mhos/m fits the data much more closely. The shape of the curves appears to be a very good fit, but there is a definite discrepancy between the experimental and

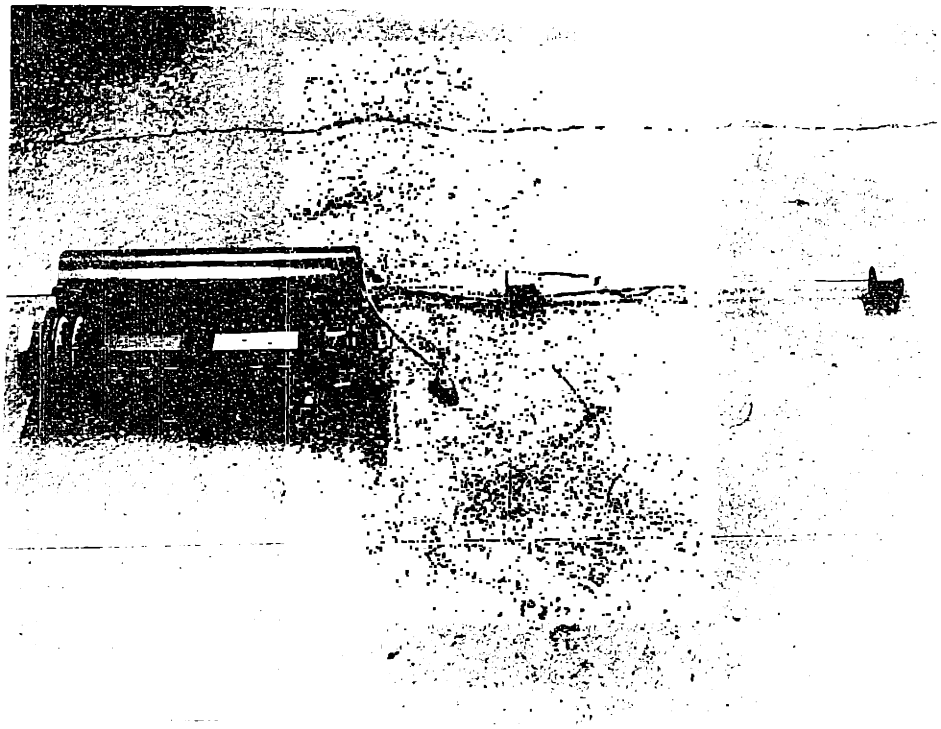

FIGURE 4.6
TRANSMITTER HOUSING

The first series of measurements was taken with the receiving antenna 1 meter below the surface. The field was measured first as the transmitter was lowered into the water, and then again as it was raised. Figure 4.7 shows a plot of the experimental data, and theoretical curves for conductivities of 4.2 mhos/m and 3.57 mhos/m. From the water temperature on the day of the experiment, and the water density on the previous day (density for the day of the experiment was not available, but the two should be quite close), the conductivity was calculated[14,15] to be approximately 4.2 mhos/m. From the plot, it is clear that 3.57 mhos/m fits the data much more closely. The shape of the curves appears to be a very good fit, but there is a definite discrepancy between the experimental and

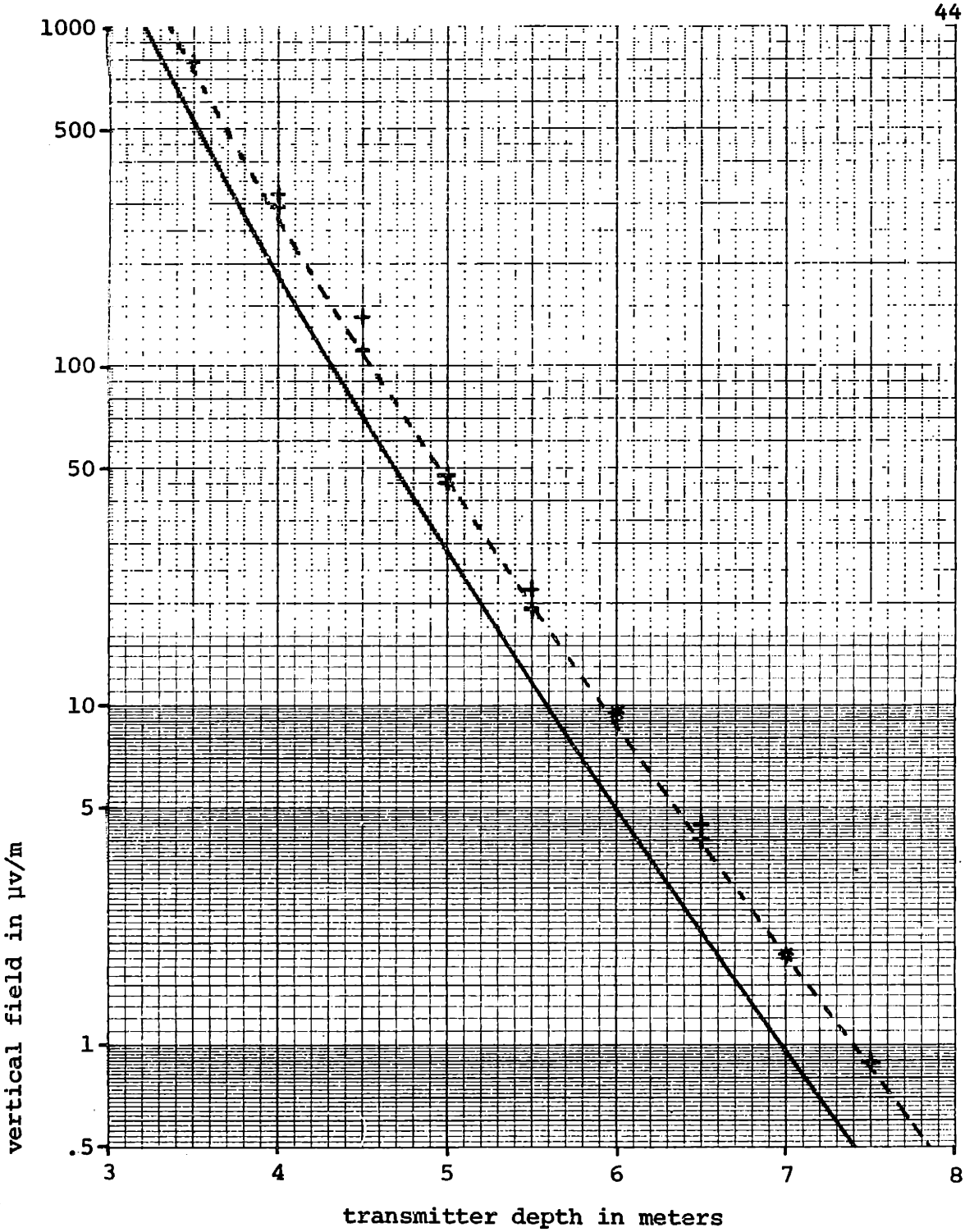

FIGURE 4.7
VERTICAL FIELD WITH RECEIVER AT 1 METER

theoretical values. It seems exceedingly unlikely that the conductivity calculation could be off by enough to make up the difference.

A second series of measurements was taken under identical conditions except that the receiver was located only $\frac{1}{2}$ meter below the surface. The results of this test are shown in Figure 4.8 along with curves for conductivities of 4.2 and 3.57 mhos/m. The curve for 3.57 mhos/m has shifted down slightly, and no longer fits the experimental values as well as before.

Because the discrepancy between the predicted and experimental values increases as the receiver is moved closer to the surface, it was thought that the difference could be the result of using a receiving antenna length comparable to the antenna depth. The potential difference between the antenna electrodes is equal to the line-integral of the electric field along the length of the antenna. If the electric field is close to being a linear function of distance over the space between the electrodes, then the field at the center of the antenna can be accurately approximated by dividing the voltage between the electrodes by the distance between them. However, if the strength of the field changes in a rapid nonlinear manner over the length of the antenna, this approximation will give inaccurate results.

In order to check this possibility, the computer program was used to calculate the strength of the field at the ends of the antenna for both antenna depths. These results were compared with the field strength at the center of the antenna to determine how nonlinear the

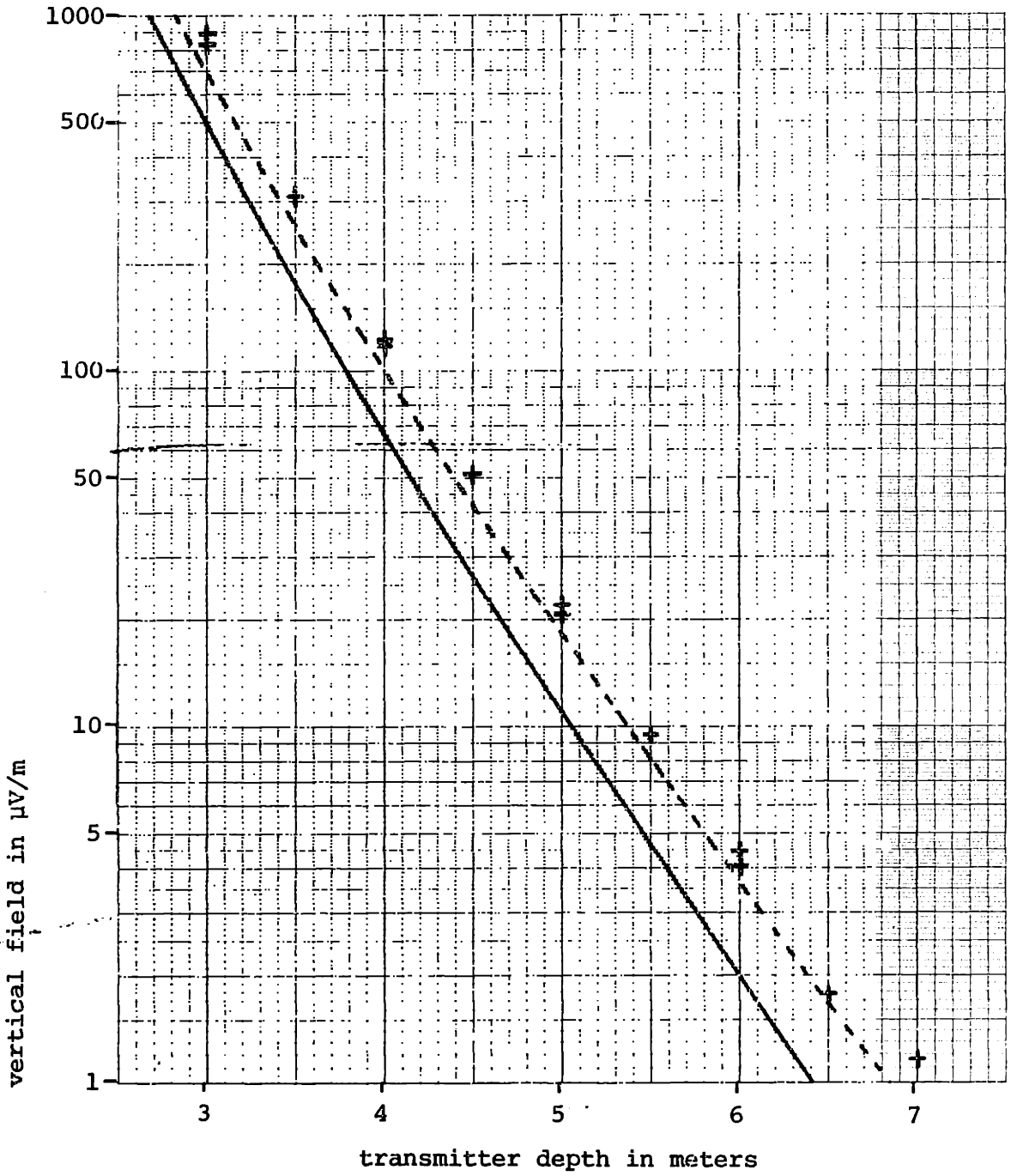

\+ experimental

—— theoretical ($\sigma = 4.2$ mhos/m)

--- theoretical ($\sigma = 3.57$ mhos/m)

FIGURE 4.8
VERTICAL FIELD WITH RECEIVER AT $\frac{1}{2}$ METER

field was over the distance between the electrodes. For all of the values of transmitter and receiver depths, the field varied only enough to introduce about a 5% increase in the theoretical values that should have been measured on the antenna. Therefore, the discrepancy cannot be the result of the large receiving antenna size. Because the error changes with receiver depth, the problem cannot be completely attributed to some error in evaluating the conductivity, either.

The error makes very little difference on a practical level. For example, at $7\frac{1}{2}$ meters transmitter depth and the receiver at 1 meter depth, the discrepancy amounts to only $\frac{1}{3}$ of a meter additional depth to get the same signal strength. It is interesting to note that the actual measured signal is always *greater* than that predicted by theory.

Because there is no surface wave phenomenon to strengthen the field (see Chapter 6), the field attenuates very rapidly down into the water. For the experimental setup used here, increasing the power by a factor of 25 (by increasing the current by a factor of 5) will increase the field by 5, and gain approximately 1 meter of range (assuming a fixed receiver sensitivity). Unless low frequencies and high power levels are used, the range of any vertical transmission system using this approach will be quite limited.

CHAPTER 5

NOISE MEASUREMENTS

The design of a practical communications system requires a thorough knowledge of the general characteristics of the noise present in the "channel." Information concerning its strength, dependence on frequency, and origin can be used to develop optimum communications equipment for a particular application.

The purpose of the noise measurements was to determine the properties of the signal present on an antenna near the surface, such as might be used for receiving signals from a submerged instrument package. Tests were done to measure the strength and spectral dependence as a function of depth and antenna orientation between 1 kHz and 100 kHz.

A considerable amount of work has been done on the design of low noise electrode-pair antennas for submarine communications. One of the major noise sources in Extremely Low Frequency (ELF) communications with this sort of antenna appears to be the result of motion modulating the corrosion currents present on the electrodes.[16] Copper electrodes were found to have a low impedance due to conducting oxides which form on the surface of the electrode (which makes them useful for transmitting), but the Velocity Induced Electrode Noise (VIEN) was fairly high compared to other metals. Fortunately, VIEN is proportional to length (L), velocity to the fifth power (V^5), and frequency to the inverse fourth power (ω^{-4}).[17] By using a one-half

meter antenna at frequencies greater than 1 kHz in slow-moving water, the VIEN should be reduced significantly to allow the use of copper electrode material. The actual antenna used consisted of two pieces of $1\frac{1}{2}$ inch diameter copper pipe $1\frac{1}{2}$ inches long, fastened with nylon bolts to a half-meter plastic rod. The antenna cable consisted of approximately five meters of shielded audio cable soldered to the electrodes. The impedance of the antenna at 1 kHz was 2 ohms.

The preamplifier used was a special low-noise design shown in Figure 5.1. By using an input transformer and low-noise semiconductors, the noise of the amplifier (referred to the input) is considerably lower than the Johnson noise of the 2 ohm source impedance, .179 nanovolts per root hertz ($nV/\sqrt{Hz}$).

The input transformer T1 has a high turns ratio (1:100) to get as much "noise free" voltage gain as possible. In order to obtain a flat frequency response over the required range, it was necessary to use two layers of 2 mil polyester tape between secondary winding layers, and to ground the inside layer of the secondary in order to keep the interwinding and interlayer capacitances down.

The initial amplification stage consists of an F.E.T. with a current source load. This gain stage is incorporated in a feedback loop including the first operational amplifier. The F.E.T. is biased at about one milliampere. Under these conditions, the incremental drain impedance is about 8 $k\Omega$, and the F.E.T. stage has a voltage gain of about 50. The voltage noise of the F.E.T. is around 2 $nV/\sqrt{Hz}$, so the noise voltage from the F.E.T. at the point A is 100 $nV/\sqrt{Hz}$. The noise voltage referred to point A from the operational amplifier is

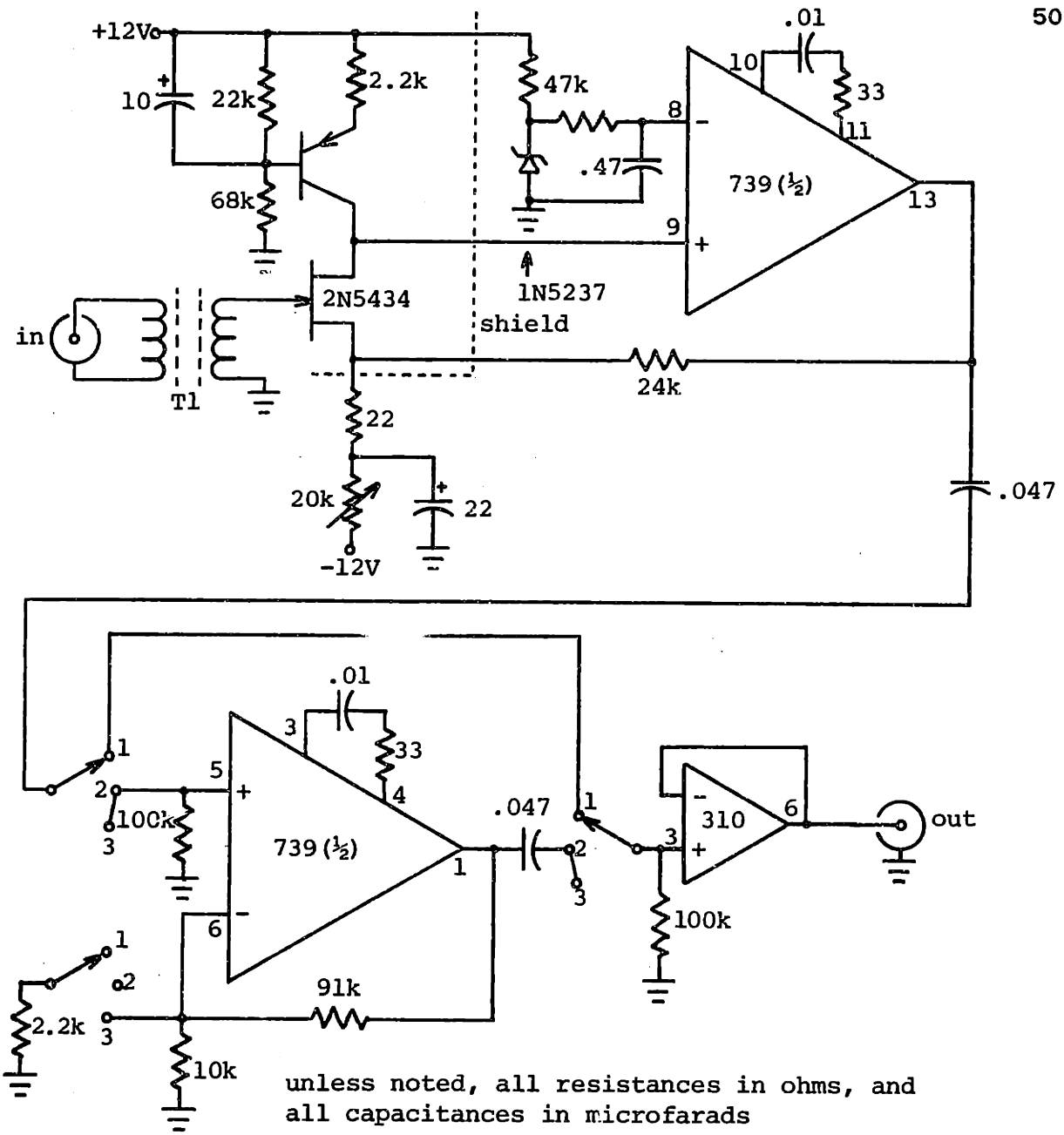

unless noted, all resistances in ohms, and all capacitances in microfarads

Gain 1 = 8×10^5

Gain 2 = $.95 \times 10^6$

Gain 3 = 4.5×10^6

T1 = 12 turns #20:1200 turns #36
Ferroxcube 3622 core
3B7 ferrite

FIGURE 5.1
LOW-NOISE PREAMPLIFIER SCHEMATIC

5 nV/$\sqrt{Hz}$. The noise voltage at point A from the current source is the transistor noise voltage (2 nV/$\sqrt{Hz}$) times its gain to point A (about 4), or 8 nV/$\sqrt{Hz}$. Assuming that the three sources are uncorrelated, this gives a total noise at the point A of only slightly more than the noise from the F.E.T. alone. When this voltage is referred to the input of the transformer, the result is a total input noise of about .02 nV/$\sqrt{Hz}$, or around 12% of the Johnson noise at the input.

The large feedback loop around the input circuitry provides a gain of about 1,000. The remaining amplifiers provide additional gain and buffering for the output. The gain of the entire circuit can be selected at either $.98 \times 10^5$, $.95 \times 10^6$, or 4.5×10^6.

The overall frequency response is flat to within minus ten percent at 1 kHz to plus ten percent at 100 kHz. The low frequency cutoffs of the input transformer and the a.c. coupling between stages were chosen to reject 60 Hz signals as much as possible. The power source used for the actual measurements consisted of four 6-volt lantern batteries to allow isolation from the power lines. An internal copper shield isolating the input was required to prevent spurious oscillations (see Figure 5.2).

Originally, it was thought that the 60 Hz noise level near shore would be sufficiently high to overdrive the input stage, and that it would be necessary to take the measurements off shore. Fortunately, tests showed that the 60 Hz rejection of the amplifier was sufficient to allow doing the experiments directly off the W.H.O.I. dock. In order to avoid electrical noise generated by work going on at Woods

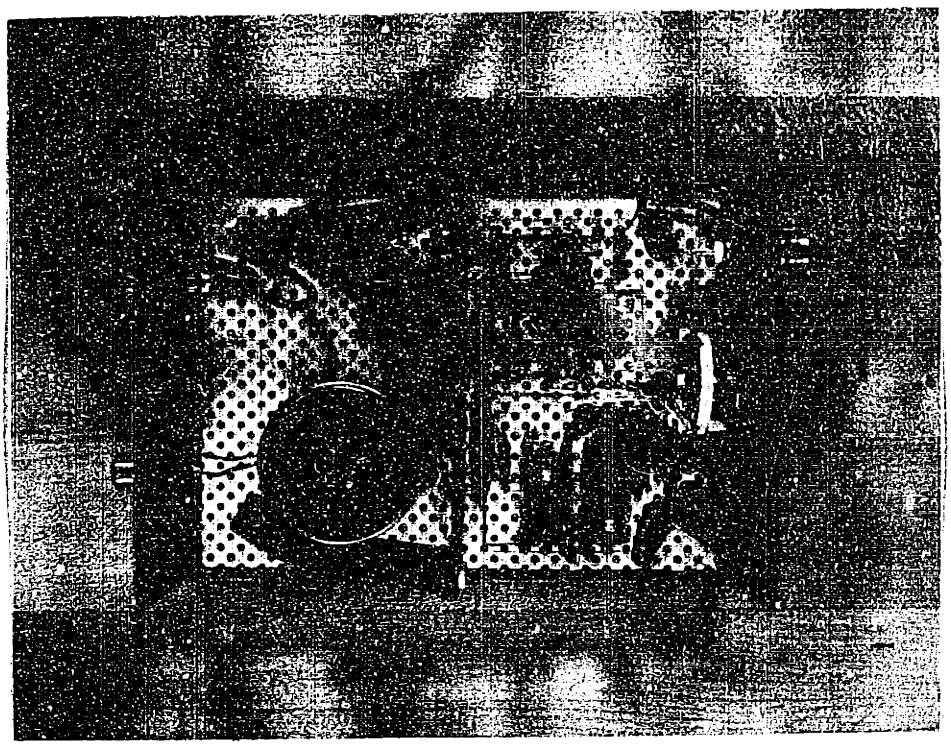

FIGURE 5.2
LOW-NOISE PREAMPLIFIER
(input section with transformer on left)

Hole, the measurements were done between the hours of 5 and 9 a.m. on a Sunday morning.

The spectral characteristics of the amplified signal were measured using a Rockland FFT 512/S real-time spectrum analyzer. This instrument measures the signal present in 400 digitally-filtered bands over the frequency range of the measurement (up to 100 kHz). The noise voltage in volts per root Hz ($V/\sqrt{Hz}$) is obtained by dividing the voltage by the square root of a single pass-band width. For example, if the full-scale frequency is 100 kHz, each band is 250 Hz wide, and the noise voltage is the display voltage times .063. The spectrum analyzer can also average many individual spectra. Connections are

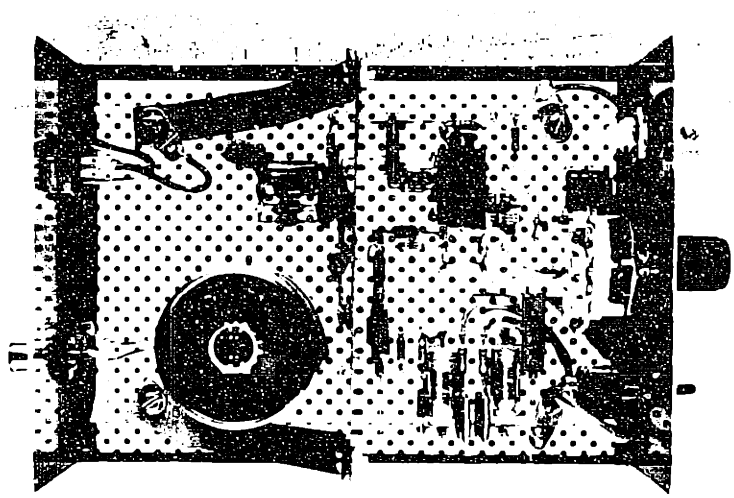

FIGURE 5.2
LOW-NOISE PREAMPLIFIER
(input section with transformer on left)

Hole, the measurements were done between the hours of 5 and 9 a.m. on a Sunday morning.

The spectral characteristics of the amplified signal were measured using a Rockland FFT 512/S real-time spectrum analyzer. This instrument measures the signal present in 400 digitally-filtered bands over the frequency range of the measurement (up to 100 kHz). The noise voltage in volts per root Hz ($V/\sqrt{Hz}$) is obtained by dividing the voltage by the square root of a single pass-band width. For example, if the full-scale frequency is 100 kHz, each band is 250 Hz wide, and the noise voltage is the display voltage times .063. The spectrum analyzer can also average many individual spectra. Connections are

available for easy interfacing with an X-Y plotter, and a Hewlett-Packard 135 AM plotter was used to produce graphs of the measurements.

Before the actual experiments were run, a measurement of the preamplifier noise was performed by putting a 2Ω carbon film resistor on the input. The resulting spectrum is shown in Figure 5.3. The vertical scale has been calibrated in $nV/\sqrt{Hz}$, and the plot is of the average of 32 separate spectra from 0 to 100 kHz. The theoretical noise from a 2Ω source is .18 $nV/\sqrt{Hz}$, which matches quite well with the measured value. A similar test was done with a resistor connected to the antenna and cable, with identical results. There were no noticeable signs of interference from manmade sources, or of noise being added to the measurement by the electronics.

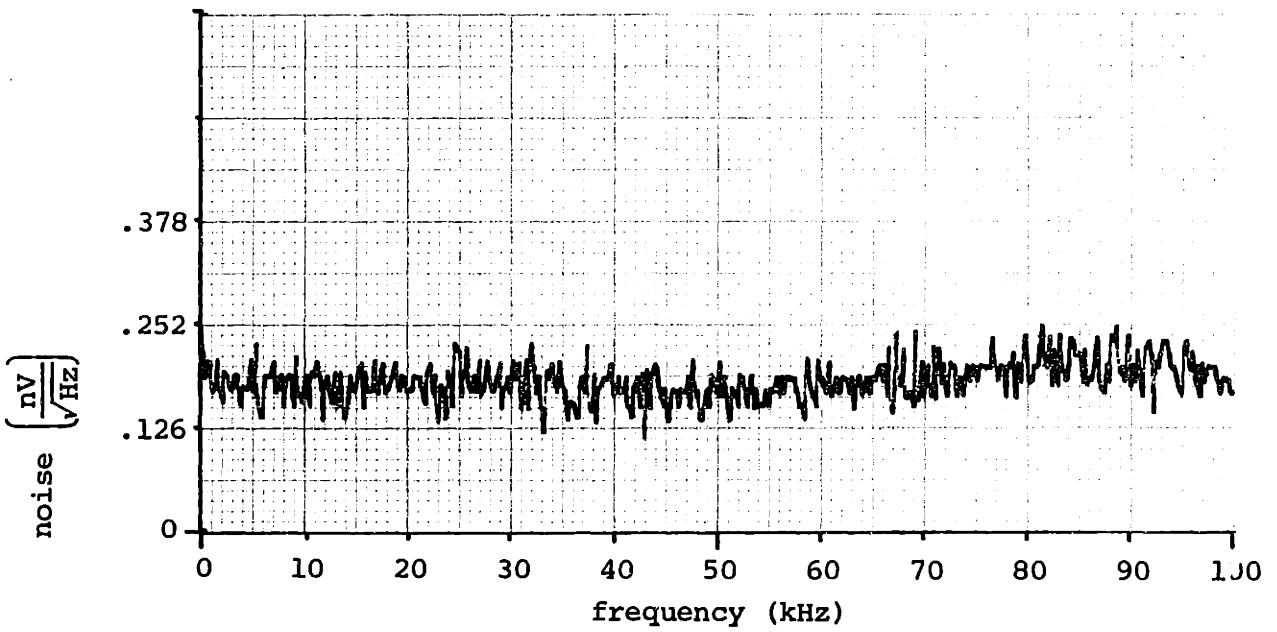

FIGURE 5.3
NOISE FROM 2Ω SOURCE RESISTOR

The first series of actual measurements was done with the antenna in a horizontal position. The spectra were plotted at 1, 2, 3, and 4 meters depth. The results at 1 and 4 meters are shown for comparison in Figures 5.4 and 5.5. The plots are averages of 256 spectra taken consecutively at 4 milliseconds per spectrum.

A number of interesting observations can be made concerning the general character of the noise from these plots. First, the noise above 30 kHz appears to have a moderately flat spectrum except for several strong narrow-band signals. The background noise is considerably stronger than the Johnson noise associated with the antenna impedance, and it does not attenuate appreciably at high frequencies. If the noise was propagating from distant sources as a plane wave, it should fall off with distance and frequency at a rate determined by the skin depth $\delta = (\omega\sigma\mu/2)^{-\frac{1}{2}}$. This lack of attenuation is particularly puzzling when the behavior of the narrow band signals as a function of depth is considered. If the signals are propagating down into the water from some manmade source above the surface, they should be severely attenuated as the depth increases from 1 to 4 meters. For example, at 95 kHz, the skin depth is .82 meters, and the signal at that frequency should be attenuated by $\exp((d_1-d_2)/\delta) = .026$. The signal is reduced in amplitude by only about a factor of 2, but the signals at 90 kHz and 93 kHz are actually *stronger* at 4 meters than at 1 meter.

The signals appear to be narrow band, and their frequencies were constant throughout the course of the experiments, which would tend to indicate that they are manmade. The signals maintained roughly the

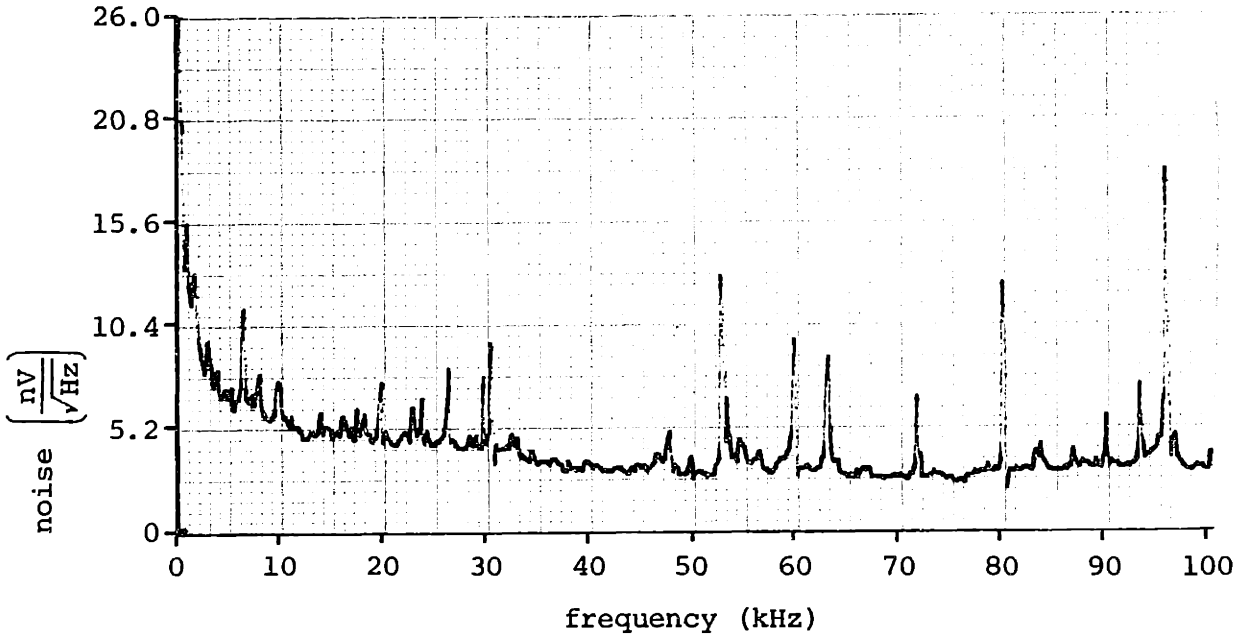

FIGURE 5.4
NOISE VOLTAGE FOR $\frac{1}{2}$ METER HORIZONTAL ANTENNA AT 1 METER

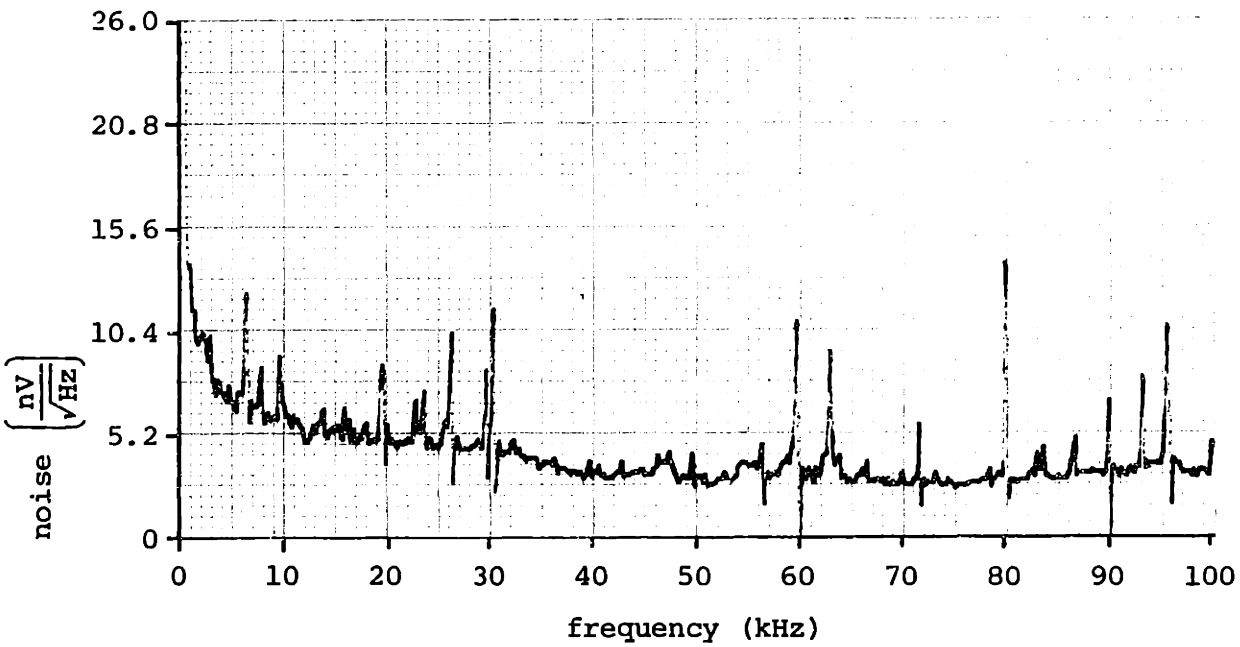

FIGURE 5.5
NOISE VOLTAGE FOR $\frac{1}{2}$ METER HORIZONTAL ANTENNA AT 4 METERS

same amplitude from measurement to measurement, except for the signal at 53 kHz at 1 meter depth, which was only present during the measurements at 1 and 2 meter depths. There are no public or private radio sources licensed to operate on the frequencies received,[18] although the military does operate stations in this frequency range. However, this would still not explain the lack of attenuation at increasing depth.

The absence of attenuation would tend to support the theory that the signal sources were in the water, either of a biological nature, or perhaps some sort of unusual V.I.E.N. phenomena. Fish are known to produce electrical signals at various frequencies, but in the form of pulses and "chatter"[18] which would tend to be more broadband than the signals measured. If the flow of water past the antenna excited a small high frequency modulation of the corrosion currents present on the electrodes, signals similar to those observed could be produced. However, it is unlikely that either of these sources would abruptly "turn off" the way the 53 kHz signal did. One possible source which would fit the measurements is acoustically generated V.I.E.N. resulting from nearby narrow band sound sources which may have been in use around the W.H.O.I. dock area.

The next set of measurements was taken with a vertical antenna at 1, 2, 3, and 4 meters depth. The spectrum plots for 1 and 4 meters are shown in Figures 5.6 and 5.7 respectively.

The overall characteristics of the spectrum are very close to those for the horizontal antenna, indicating that the noise field is omnidirectional. With the exception of the 53 kHz signal, all of the

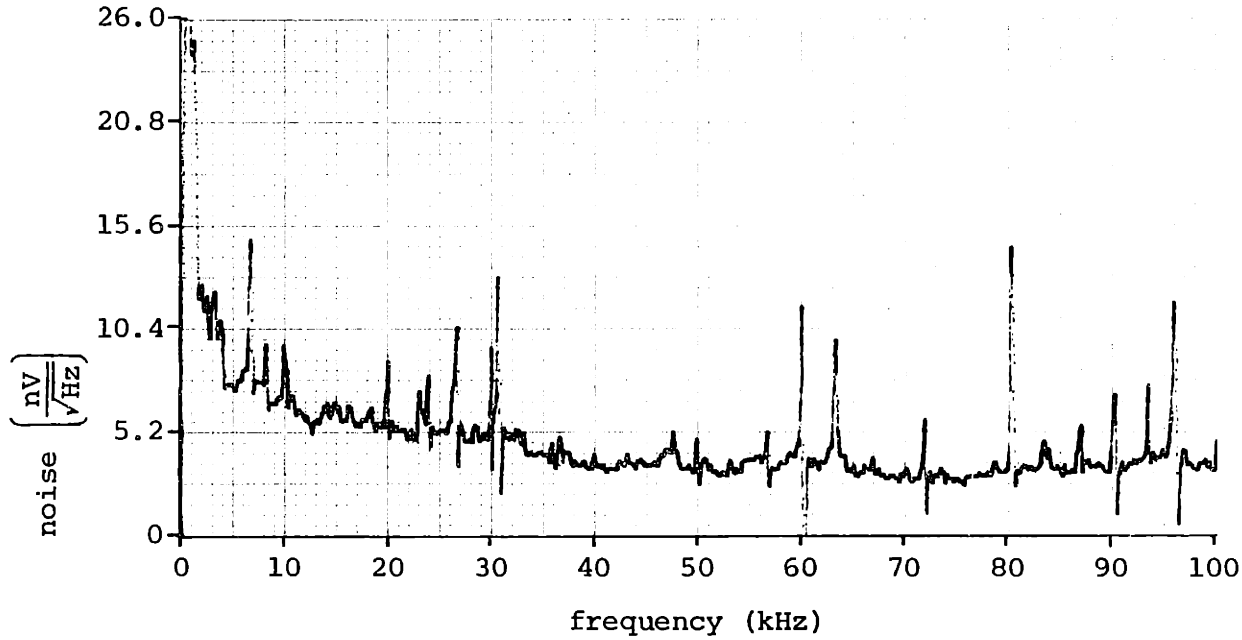

FIGURE 5.6
NOISE VOLTAGE FOR $\frac{1}{2}$ METER VERTICAL ANTENNA AT 1 METER

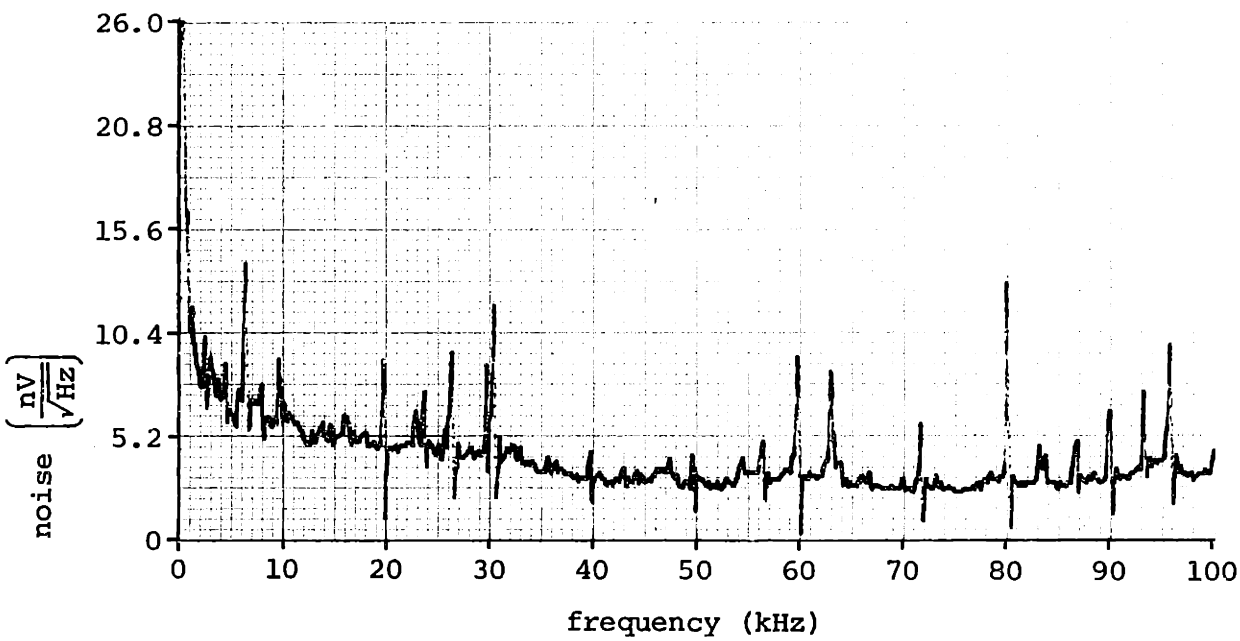

FIGURE 5.7
NOISE VOLTAGE FOR $\frac{1}{2}$ METER VERTICAL ANTENNA AT 4 METERS

narrow-band signals are present with approximately the same strength as before. There is no appreciable difference in the signal strengths between 1 and 4 meter depths.

All of the preceding measurements suffer from an apparent increase in the noise level at low frequencies. This was thought to be an artifact of the spectrum analyzer characteristics in the presence of a very strong 60 Hz signal, possibly the result of side lobe leakage in the digital filtering process. Because of this problem, a more detailed measurement of the low frequencies was done over several of the spectrum analyzer's lower frequency ranges. The results of these measurements are shown in Figures 5.8 through 5.11 (again averaged over 256 spectra).

A direct comparison of these plots is somewhat difficult because of the different scale factors required by the changing filter bandwidth. A check of the noise levels indicated for 9 kHz shows a reading of about 6 nV/$\sqrt{\text{Hz}}$ on the 50 kHz spectrum plot, as compared to 6.3 nV/$\sqrt{\text{Hz}}$ on the 20 kHz plot and 6.5 nV/$\sqrt{\text{Hz}}$ on the 10 kHz plot. This shows that the increase in noise at low frequencies is real, which is reasonable considering the attenuation of high frequencies in a dissipative medium. The difference, however, is not very large. The average background noise level around 100 kHz is about 3.4 nV/$\sqrt{\text{Hz}}$ as compared to about 10 nV/$\sqrt{\text{Hz}}$ around 2 kHz. Although this amounts to roughly a factor of ten drop in power, it is far less than the difference one would expect if the signals had propagated any great distance, which implies that the high frequency noise must originate at or near the antenna electrodes.

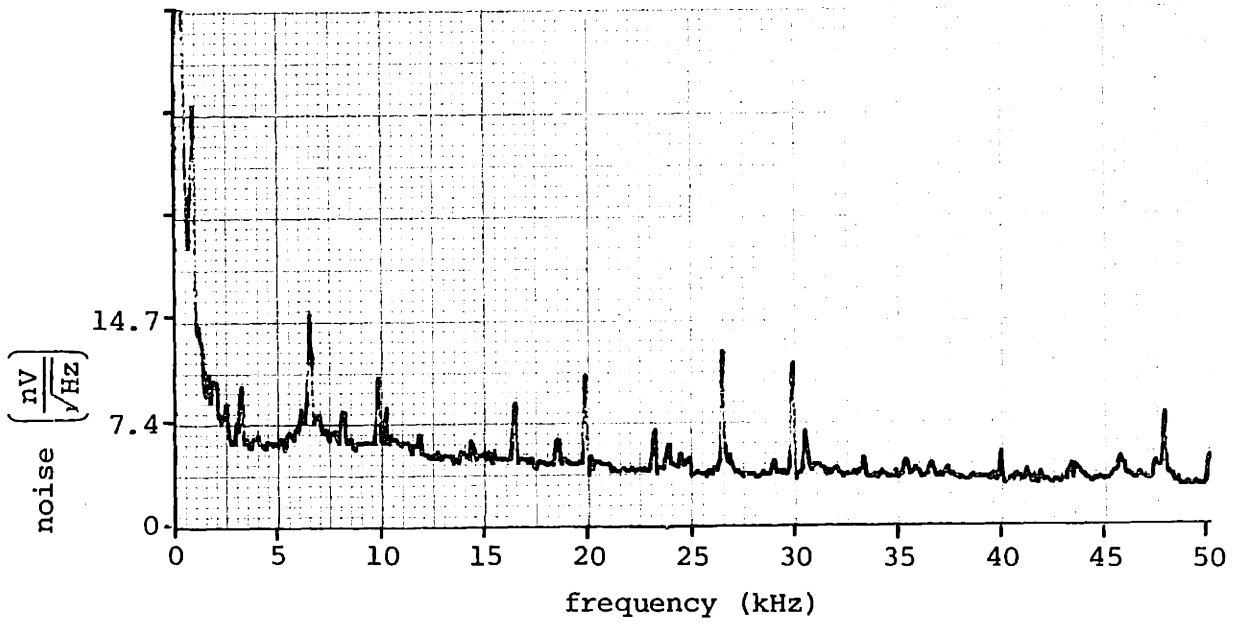

FIGURE 5.8
VERTICAL ANTENNA NOISE AT 4 METERS FROM 0 TO 50 KHZ

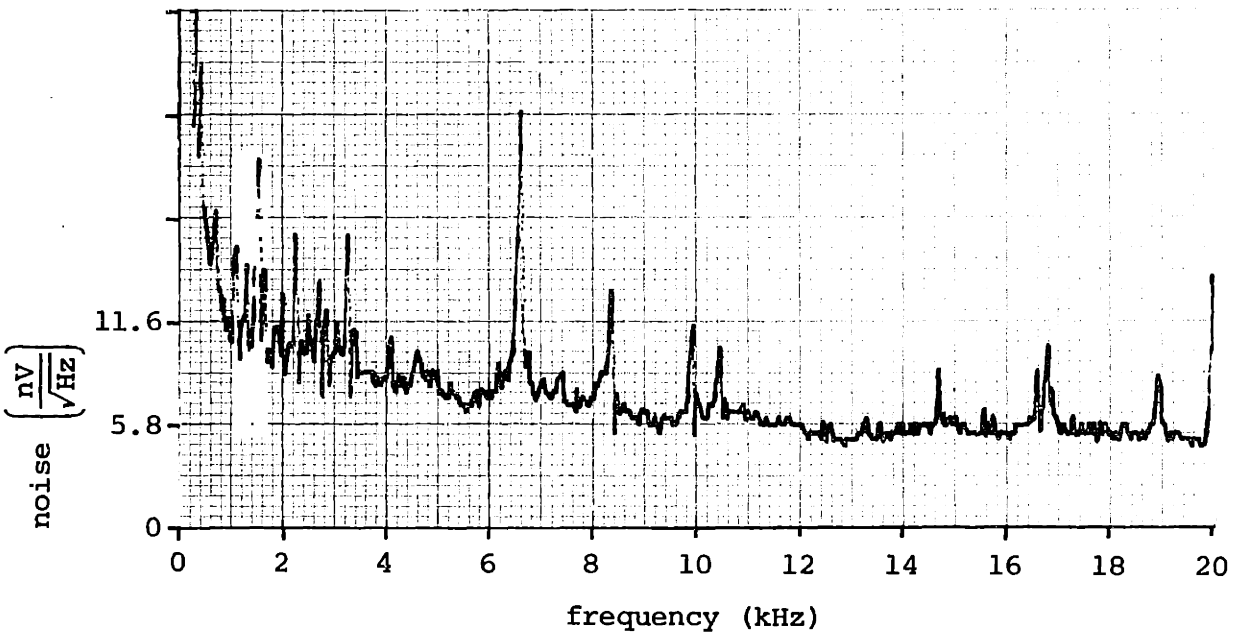

FIGURE 5.9
VERTICAL ANTENNA NOISE AT 4 METERS FROM 0 TO 20 KHZ

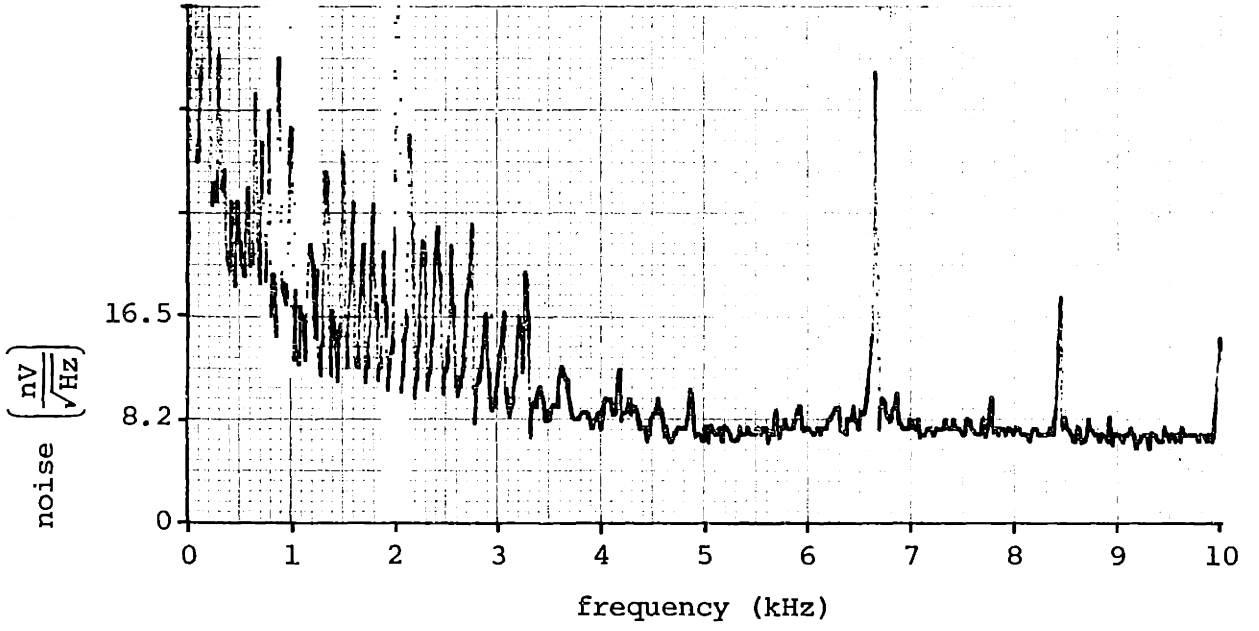

FIGURE 5.10
VERTICAL ANTENNA NOISE AT 4 METERS FROM 0 TO 10 KHZ

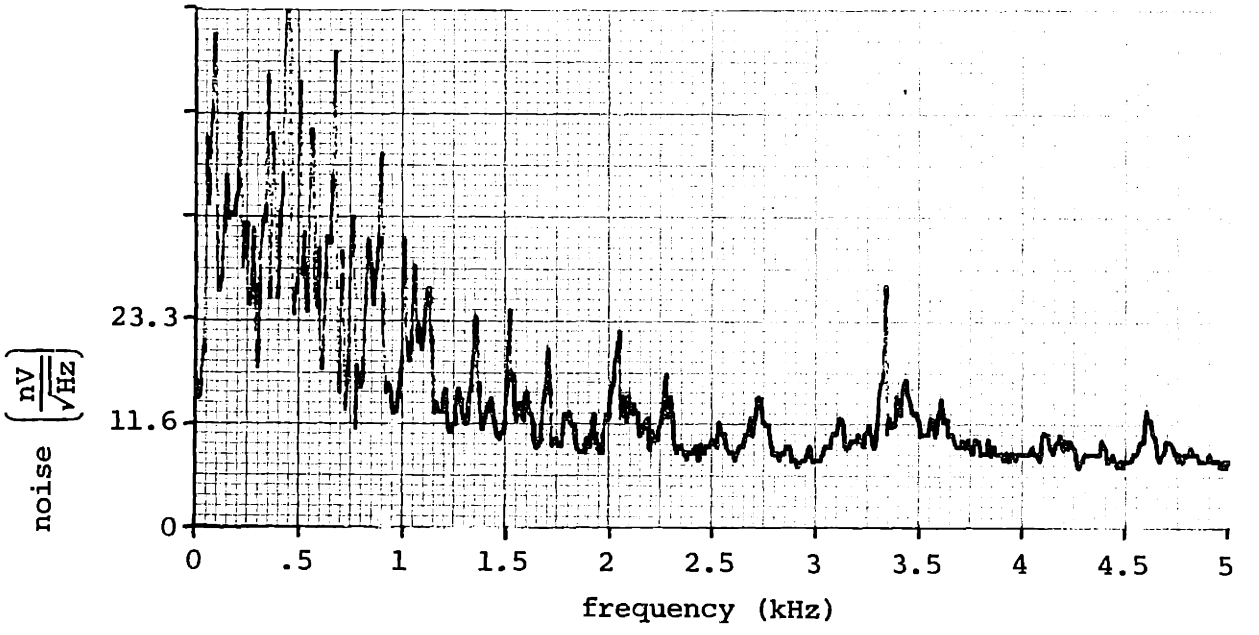

FIGURE 5.11
VERTICAL ANTENNA NOISE AT 4 METERS FROM 0 TO 5 KHZ

The overall noise appears to be the sum of a moderately flat background noise component and a large number of stronger narrow-band signals. Because the narrow-band signals do not seem to vary in frequency a great deal, it should be possible to design communications systems which avoid these strong sources of interference even if their exact nature is not fully understood.

CHAPTER 6

CHANNEL CAPACITY ANALYSIS

Using the results of the noise measurements described in Chapter 5, estimates can be made of the characteristics of a communications "channel" implemented with the type of signaling system under consideration. Because the analysis and experiments have been restricted to transmitting short single tones, no information is available concerning the dispersion and fading characteristics of the channel, and they will be neglected in this analysis. Mathematical techniques exist for handling these more complex cases,[20] should they prove to be a problem.

Over the range of 1 to 100 kHz, the background noise (avoiding sources of narrow band interference) is moderately frequency independent, especially when viewed over a band small compared to its center frequency. If the ocean is modeled as a simple additive Gaussian white noise channel (for lack of any better model, and for computational ease), then the channel capacity can be calculated using the Shannon capacity theorem:[21]

$$R < W \log_2 \left(1 + \frac{P_S}{W N_0} \right) , \qquad [6.1]$$

where:

R is the maximum transmission rate for reliable communication in bits per second,

W is the bandwidth of the signal in hertz,

P_S is the average power in the received signal in watts, and

N_0 is the "noise power" of the Gaussian white noise in watts per hertz.

N_0 is defined to be equal to twice the power spectral density $S_w(f)$ of the signal at the antenna. $S_w(f)$ is proportional to V_n^2 (the noise voltage at the antenna in $nV/\sqrt{Hz}$ squared) with the same proportionality factor which relates the power of the signal P_S to the square of the signal voltage at the antenna, V_s^2 (in $(nV)^2$).

This allows the channel capacity to be rewritten in the following form (after cancelling the proportionality constant from P_S and N_0):

$$R < W \log_2 \left(1 + \frac{V_s^2}{2 W V_n^2} \right) . \qquad [6.2]$$

This allows calculation of the channel capacity in terms of known variables, assuming the signal voltage is obtained for the same antenna design with which the noise voltage was measured.

Before calculations of the channel capacity can be done, the frequency characteristics of the channel must be considered. Figure 6.1 shows the attenuation as a function of frequency for vertical transmission at two different ranges. The transmitter was assumed to be a 1 ampere source driving a vertical $\frac{1}{2}$ meter antenna, and the receiver was assumed to be a $\frac{1}{2}$ meter vertical antenna at 1 meter

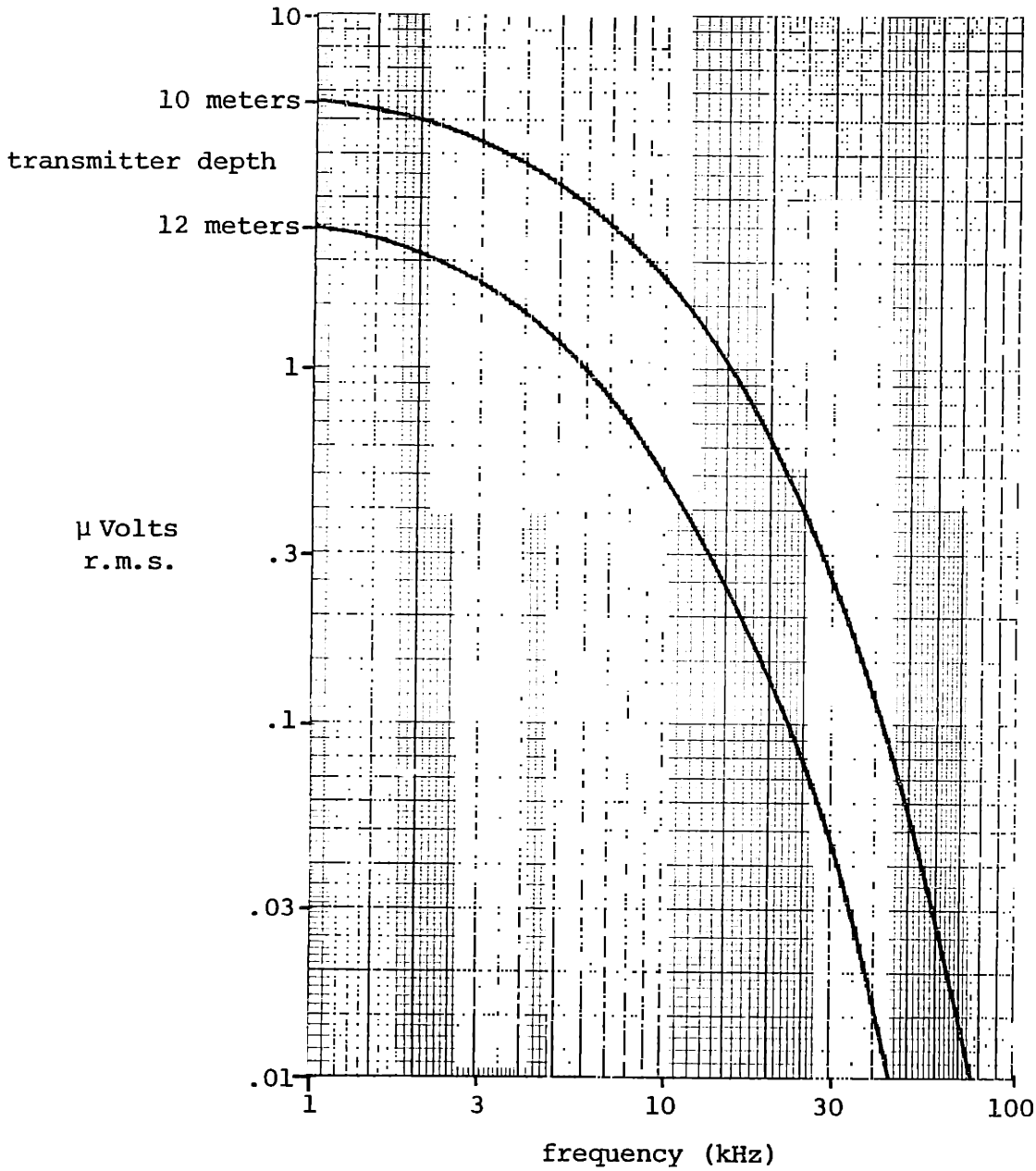

FIGURE 6.1
SIGNAL ATTENUATION WITH FREQUENCY
(receiver depth = 1 meter)

depth. The upper curve is for a transmitter depth of 10 meters, and the lower curve for a transmitter depth of 12 meters. The fields were calculated using the numerical integration program described earlier in Chapter 3.

The frequency characteristics of the channel are not very "flat" and vary considerably with range. The 3 db point at 10 meters depth is on the order of 3.5 kHz, as compared to about 3 kHz at 12 meters depth. The channel capacity theorem can be reformulated for a frequency-dependent channel by modeling the dependence with a linear filter, but because of complexity of modeling the frequency dependence of the ocean (which is in turn a function of range), an approximate calculation was made for narrow-band transmissions.

If the bandwidth of the transmitted signal is chosen to be a fixed small fraction of the center frequency (f_c) of the band, then the signal voltage (V_s) can be taken at f_c without introducing much error from the frequency dependence of the channel. Then, using the noise voltage at f_c, the channel capacity can be calculated as a function of the transmission bandwidth (which is directly proportional to f_c).

Figure 6.2 shows a graph of the channel capacity of a 1 ampere r.m.s. source at a depth of 10 meters transmitting to a receiver at a depth of 1 meter (both $\frac{1}{2}$ meter antennas). The channel capacity was calculated assuming the signal bandwidth to be equal to one tenth of the center frequency.

The channel capacity can be separated into two different regions as a function of bandwidth. Below a bandwidth of 1 kHz (corresponding

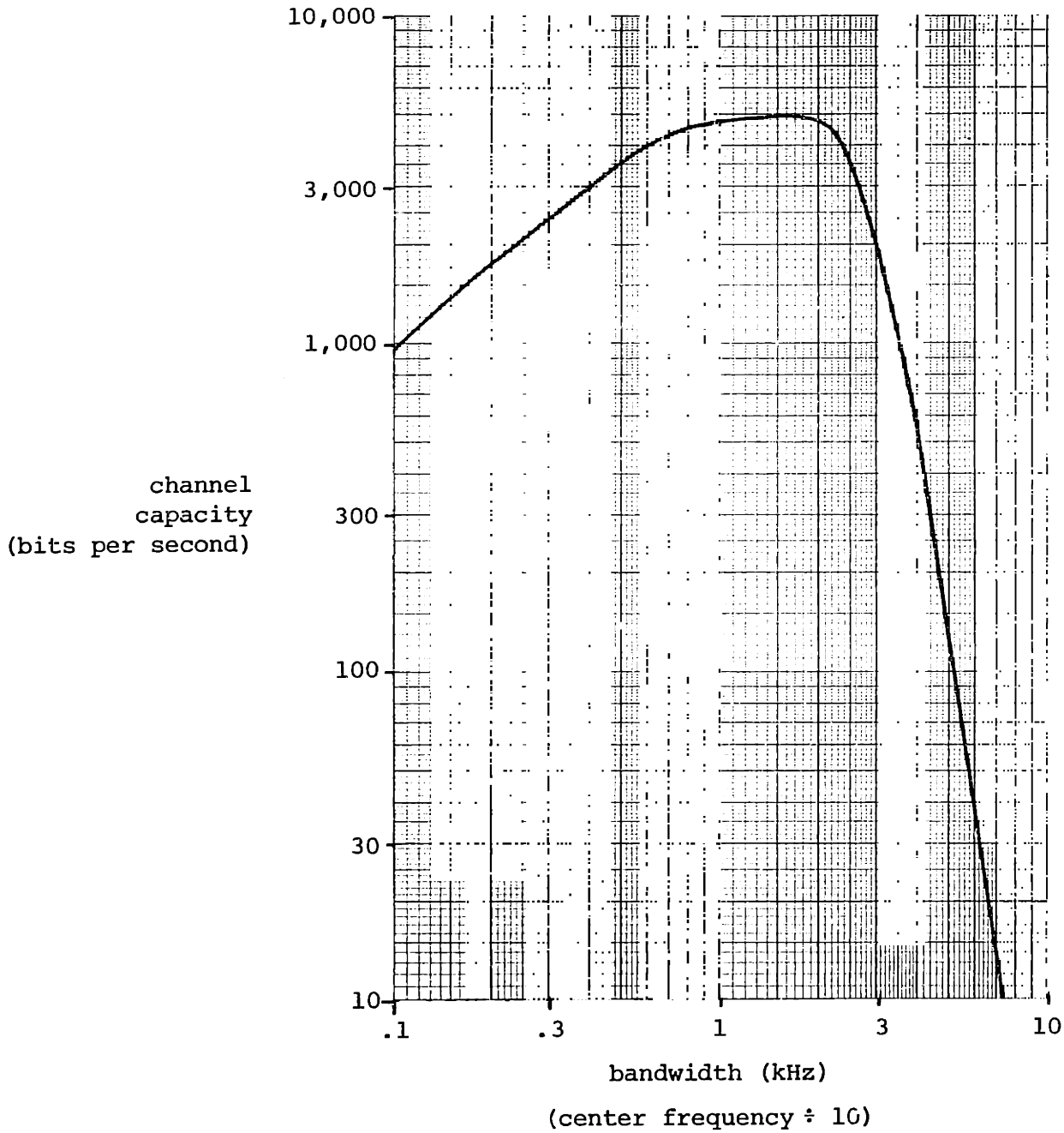

FIGURE 6.2
CHANNEL CAPACITY AS A FUNCTION OF BANDWIDTH
1 A r.m.s. source at 12 meters depth
receiver at 1 meter depth

to a center frequency of 10 kHz), the channel capacity is bandwidth limited, and the capacity can be increased by increasing the bandwidth (and center frequency) of the signal. Increasing the transmitted power in this region gives only a small increase in capacity. For bandwidths greater than about 2 kHz, increasing the bandwidth (and center frequency) *decreases* the channel capacity because the signal strength falls off so rapidly with frequency. This region is "power efficient," and the channel capacity increases roughly proportional to P_S or V_S^2, although it takes a very large increase in power to make up for the loss as higher frequencies are used.

For a fixed range, there will be an optimum bandwidth and center frequency where a further increase in frequency reduces the channel capacity, but also where the channel is sufficiently power efficient to allow improving performing by increasing the transmitter power if it is required. For the case shown in Figure 6.2, this corresponds to a bandwidth of 2 kHz and a center frequency of 20 kHz, and results in a channel capacity of about 5 thousand bits per second.

Although this may seem to be a reasonable transmission rate, the channel capacity is the maximum theoretical limit assuming "optimum receivers." A practical system does well to reach a quarter of this calculated capacity, and considering the limited range, it is not very impressive.

CHAPTER 7

INVESTIGATION OF THE FIELDS AT THE SURFACE

From a theoretical standpoint, the study of the fields observed with the source and receiver near the surface is quite complex, and it has been the focus of a great deal of research. Because of surface wave propagation effects, it is possible to send signals over distances of several hundred meters at frequencies of 100 kHz or more.

In his book, Baños derives approximate expressions for the fields near the surface using saddle point integration techniques (see Baños Chapter 4), which are valid for radial distances at least several times the wavelength of the signal in water. These results are summarized in Chapter 7 of Baños, and the equations for the radial and azimuthal fields of a horizontal electric dipole near the surface are given below (for the geometry shown in Figure 2.1):

$$E_{1r} \approx \frac{p \cos\psi}{2\pi\sigma_1 r^3} e^{ik_1(h-z)} \quad \text{, and} \qquad [7.1]$$

$$E_{1\psi} \approx \frac{p \sin\psi}{\pi\sigma_1 r^3} e^{ik_1(h-z)} \quad , \qquad [7.2]$$

where:

$i = \sqrt{-1}$,

p is the dipole moment of the source,

h is the transmitter depth,

$-z$ is the receiver depth,

σ is the conductivity of the water,

r is the transmitter-receiver separation,

ψ is the angle between the axis of the transmitting antenna and the receiver, and

k_1 is the propagation constant for water.

The source is assumed to have a harmonic time dependence of frequency ω.

Several interesting conclusions can be drawn from these two results. First, as long as both the source and receiver are close to the surface, the signal falls off only as the inverse of the radial separation cubed. The exponential attenuation of the signal usually associated with the propagation of fields in lossy media is absent.

This lack of exponential attenuation is probably the cause of a number of the promising claims made by various experimenters. If they performed their communications tests close to the surface (that being the easiest location to work at), they could have been severely misled by their findings.

The other interesting feature which equations [7.1] and [7.2] contain is an apparent "rotation" of the antenna pattern. Although the general features of the field dependence on angle are the same as for a simple static dipole, the peak azimuthal field (for $\psi = \pm\frac{\pi}{2}$) is twice as strong as the peak radial field (for $\psi = 0$ or π). This is

exactly the *opposite* of the relative peak strength of the radial and azimuthal components of a simple dipole in air (see Figure 7.1).

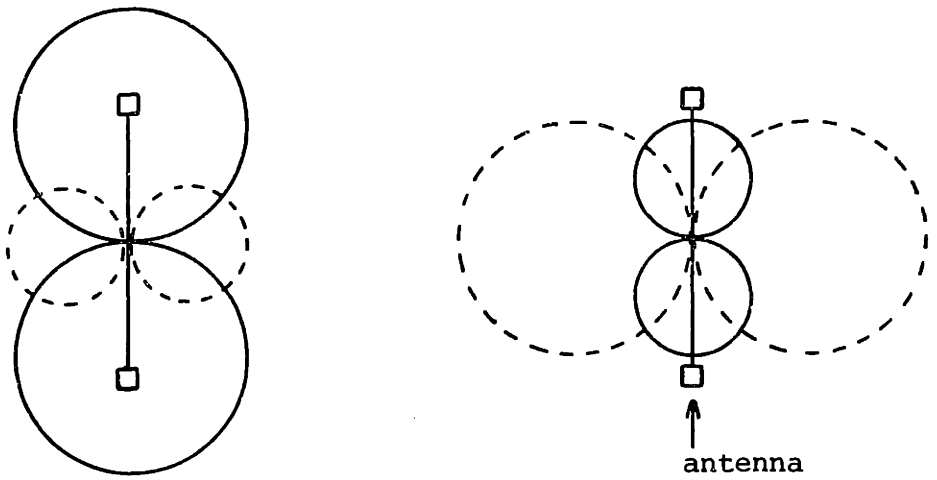

FIGURE 7.1
RELATIVE FIELD STRENGTH PATTERNS FOR NEAR SURFACE CASE

To allow measurements at shorter ranges than allowed for equations [7.1] and [7.2] to be valid, and to provide an alternate theoretical check, the fields were calculated for the case of both the transmitter and receiver at the surface ($h = z = 0$), using a "quasi-static" approach. This is done by setting the propagation constant for air (k_2) equal to zero, and is equivalent to assuming that the fields in air are quasi-static and satisfy Laplace's equation.

For a horizontal electric dipole, the field components can be

written in the following form (see Chapter 2):

$$E_{1r} = \frac{i\omega p\mu_0}{4\pi k_1^2} \cos\psi \left\{ \frac{\partial}{\partial^2} \left(G_{11} - G_{12} + k_1^2 V_{11} \right) + k_1^2 \left(G_{11} - G_{12} + U_{11} \right) \right\} \quad , \text{ and} \tag{7.3}$$

$$E_{1\psi} = -\frac{i\omega p\mu_0}{4\pi k_1^2} \sin\psi \left\{ \frac{1}{r} \frac{\partial}{\partial r} \left(G_{11} - G_{12} + k_1^2 V_{11} \right) + k_1^2 \left(G_{11} - G_{12} + U_{11} \right) \right\} \quad , \tag{7.4}$$

where:

μ_0 is the permeability of free space (and sea water),

$$G_{11} = \frac{e^{ik_1 R_1}}{R_1} \quad , \tag{7.5}$$

$$G_{12} = \frac{e^{ik_1 R_2}}{R_2} \tag{7.6}$$

$$V_{11} = \int_0^\infty \frac{2\lambda e^{-\gamma_1 (h-z)} J_0(\lambda r)\, d\lambda}{k_2^2 \gamma_1 + k_1^2 \gamma_2} \quad , \tag{7.7}$$

$$U_{11} = \int_0^\infty \frac{2\lambda e^{-\gamma_1 (h-z)} J_0(\lambda r)\, d\lambda}{\gamma_1 + \gamma_2} \tag{7.8}$$

$$\gamma_m = \left(\lambda^2 - k_m^2 \right)^{\frac{1}{2}} \quad , \; m = 1,2, \text{ and} \tag{7.9}$$

$J_0(\lambda r)$ is a Bessel function of order zero.

By setting k_2 equal to zero, noting that $h = z = 0$ and $R_1 = R_2$ at the surface (for the geometry in Figure 2.1), and making use of the formula:

$$k_1^2 \approx i\omega\mu_0\sigma \quad , \tag{7.10}$$

a number of terms will drop out of the equations for the field components. The results are listed below:

$$E_{1r} = \frac{p}{4\pi\sigma} \cos\psi \left\{ \frac{\partial}{\partial r^2} \left(k_1^2 V_{11} \right) + k_1^2 U_{11} \right\} , \text{ and} \qquad [7.11]$$

$$E_{1\psi} = \frac{p}{4\pi\sigma} \sin\psi \left\{ \frac{1}{r} \frac{\partial}{\partial r} \left(k_1^2 V_{11} \right) + k_1^2 U_{11} \right\} . \qquad [7.12]$$

The integrals have also been simplified to the following forms:

$$V_{11} = \int_0^\infty \frac{2J_0(\lambda r)\, d\lambda}{k_1^2} , \text{ and} \qquad [7.13]$$

$$U_{11} = \int_0^\infty \frac{2\lambda J_0(\lambda r)\, d\lambda}{\gamma_1 + \lambda} . \qquad [7.14]$$

Equation [7.13] can be evaluated directly, giving:

$$V_{11} = \frac{2}{k_1^2 r} \qquad [7.15]$$

An exact solution of the integral U_{11} (originally developed by van der Pol) is given in Baños as:

$$U_{11} = \frac{2}{k_1^2 - k_2^2} \frac{1}{r} \frac{\partial}{\partial r} \left(\frac{e^{ik_2 r}}{r} - \frac{e^{ik_1 r}}{r} \right) . \qquad [7.16]$$

Setting k_2 to zero reduces [7.16] to:

$$U_{11} = \frac{2}{k_1^2} \frac{1}{r} \frac{\partial}{\partial r} \left(\frac{1}{r} - \frac{e^{ik_1 r}}{r} \right) . \qquad [7.17]$$

Substituting [7.15] and [7.17] into [7.11] and [7.12], and performing the indicated partial differentiations gives these final expressions for the field components:

$$E_{1r} = \frac{p}{2\pi\sigma} \cos\psi \left\{ \frac{1}{r^3} + \frac{e^{ik_1 r}}{r^2} \left(\frac{1}{r} - ik_1 \right) \right\} , \text{ and} \qquad [7.18]$$

$$E_{1\psi} = \frac{p}{\pi\sigma} \sin\psi \left\{ \frac{1}{r^3} - \frac{e^{ik_1 r}}{2r^2} \left(\frac{1}{r} - ik_1 \right) \right\} . \qquad [7.19]$$

For $k_1 r$ much greater than one, the quasi-static field components reduce to the field components derived by Banos using the saddle point integration technique (equations [7.1] and [7.2]). The factor of 2 appears in the azimuthal term rather than the radial term, as indicated before.

During the summer of 1975, a measurement of the attenuation of the radial field at the surface was performed off the dock area at W.H.O.I., using equipment very similar in design to the transmitter and receiver used for the vertical transmission experiment described in Chapter 4. The antennas were both one meter long, and the transmitter produced an antenna current of 1 ampere peak-to-peak at a frequency of 1 kHz. From density and temperature data for the water on the day of the experiment, the conductivity was calculated to be 5 mhos/meter. A graph of the measured radial field and the theoretical quasi-static radial field are shown in Figure 7.2 for comparison. Although the curve is close to the experimental points, and the overall shape appears to be about right, the measured field is always stronger (by as much as a factor of two) than the theoretical value. This is similar to the results obtained in the vertical field experiment. Unfortunately, no measurements of the azimuthal field were made at the time.

In order to measure the relative field strengths at the surface, a pair of $\frac{1}{2}$ meter antennas (similar to those used for the experiment described in Chapter 4) were fastened 3.5 meters apart on a narrow

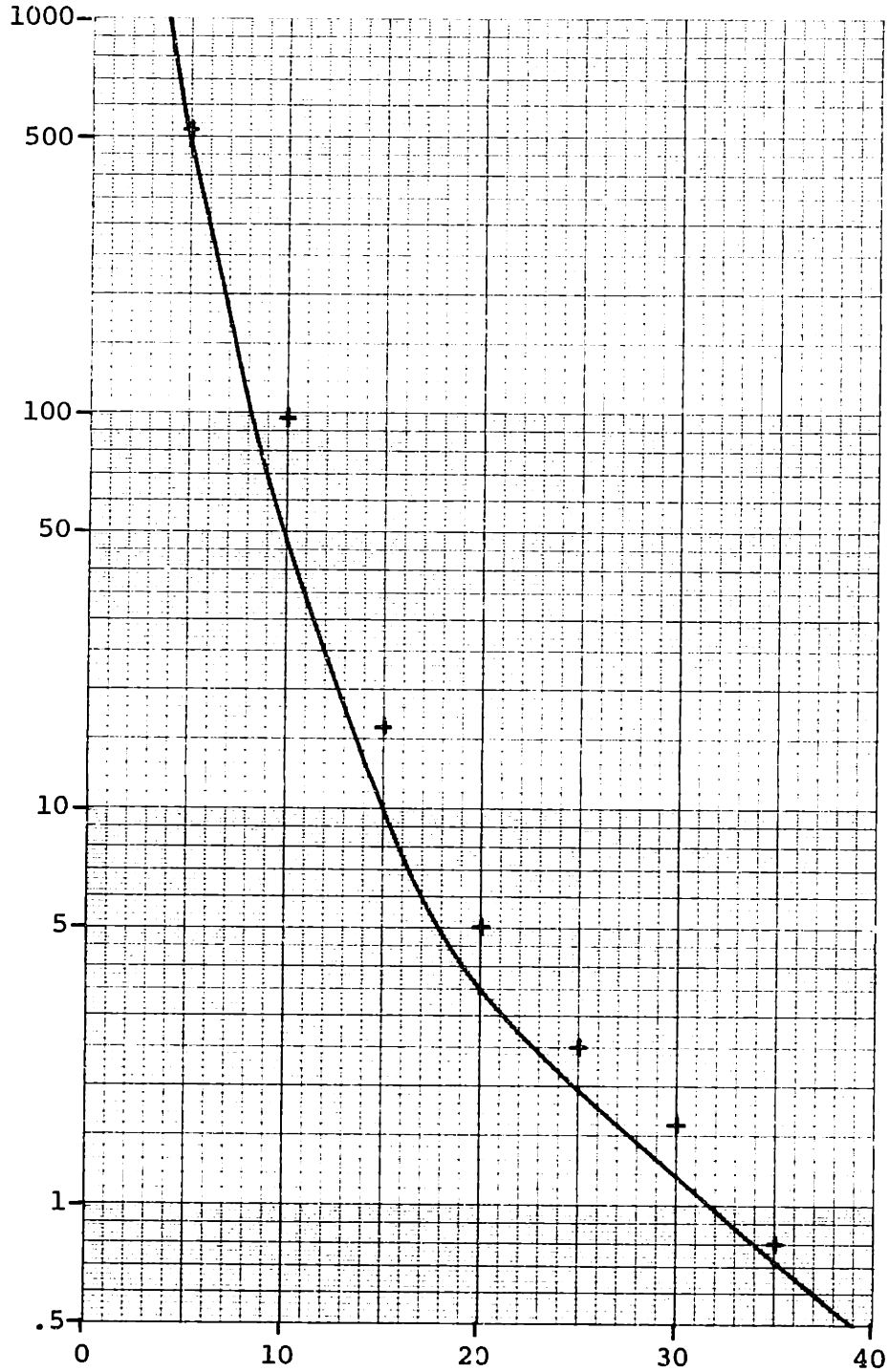

FIGURE 7.2
RADIAL FIELD AT THE SURFACE

board using plastic cable clamps in such a manner that they could be easily rotated. With the antennas aligned coaxially (see Figure 7.3a), the peak radial field could be measured, and with the antennas rotated to a "broadside" configuration, the peak azimuthal field could be measured (see Figure 7.3b). The board supplied both a rigid structure to hold the antennas in a fixed orientation and sufficient flotation to hold the electrodes just beneath the surface.

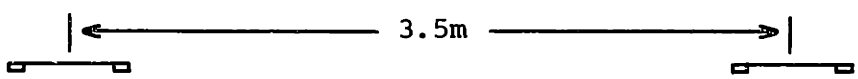

orientation for radial field measurement

(a)

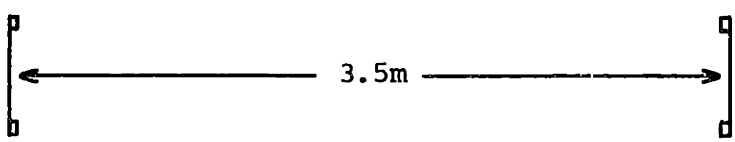

orientation for azimuthal field measurement

(b)

FIGURE 7.3
ANTENNA POSITIONS FOR PATTERN MEASUREMENT

10 kHz was selected as an operating frequency to ensure a strong signal and a wavelength of sufficient size to guarantee the validity of the short dipole model. The receiver used for the measurements was the same as used for the vertical field experiment, but modified for

use at 10 kHz. The necessary component changes are indicated on the schematic in Figure 4.2. The bandwidth of the circuit is about 700 Hz, and the gain is about a factor of 10 lower than at 100 kHz because of the lower Q of the tank circuit.

Because of the difficulty of handling the 100 kHz transmitter, and the need to keep the heatsink end of the housing immersed, a new transmitter was constructed using a μA 791 power operational amplifier. This integrated circuit has a peak output capability of 1 ampere, and adequate frequency response to be used at 10 kHz. A schematic of the transmitter is shown in Figure 7.4. The oscillator and gating circuitry are similar to those used in the 100 kHz transmitter, with the addition of the 15 kΩ resistor and 4.7 μfd capacitor. This low-pass network was necessary to avoid a destructive transient from over-driving the current source each time the oscillator turned on. The current source was the standard non-inverting type, and was set to operate at $\frac{1}{2}$ ampere r.m.s. The 2-to-1 output transformer then provided 1 ampere to the antenna. Power was supplied by four 6-volt lantern batteries. A photograph of the completed unit is shown in Figure 7.5.

Using the values $\sigma = 4$, $f = 10^4$, $r = 3.5$, and $p = \frac{1}{2}$ in equations [7.18] and [7.19] gives values of 1.38 mV/m and 1.49 mV/m for the radial and azimuthal fields respectively. When the measurements were first performed, the resulting fields were: E_{1r} = 1.88 mv/m, and $E_{1\psi}$ = 1.62 mV/m. It was thought that the antennas might be large enough compared to their separation to affect the measurement, so they were both reduced to .25 m length. The measurements were repeated in

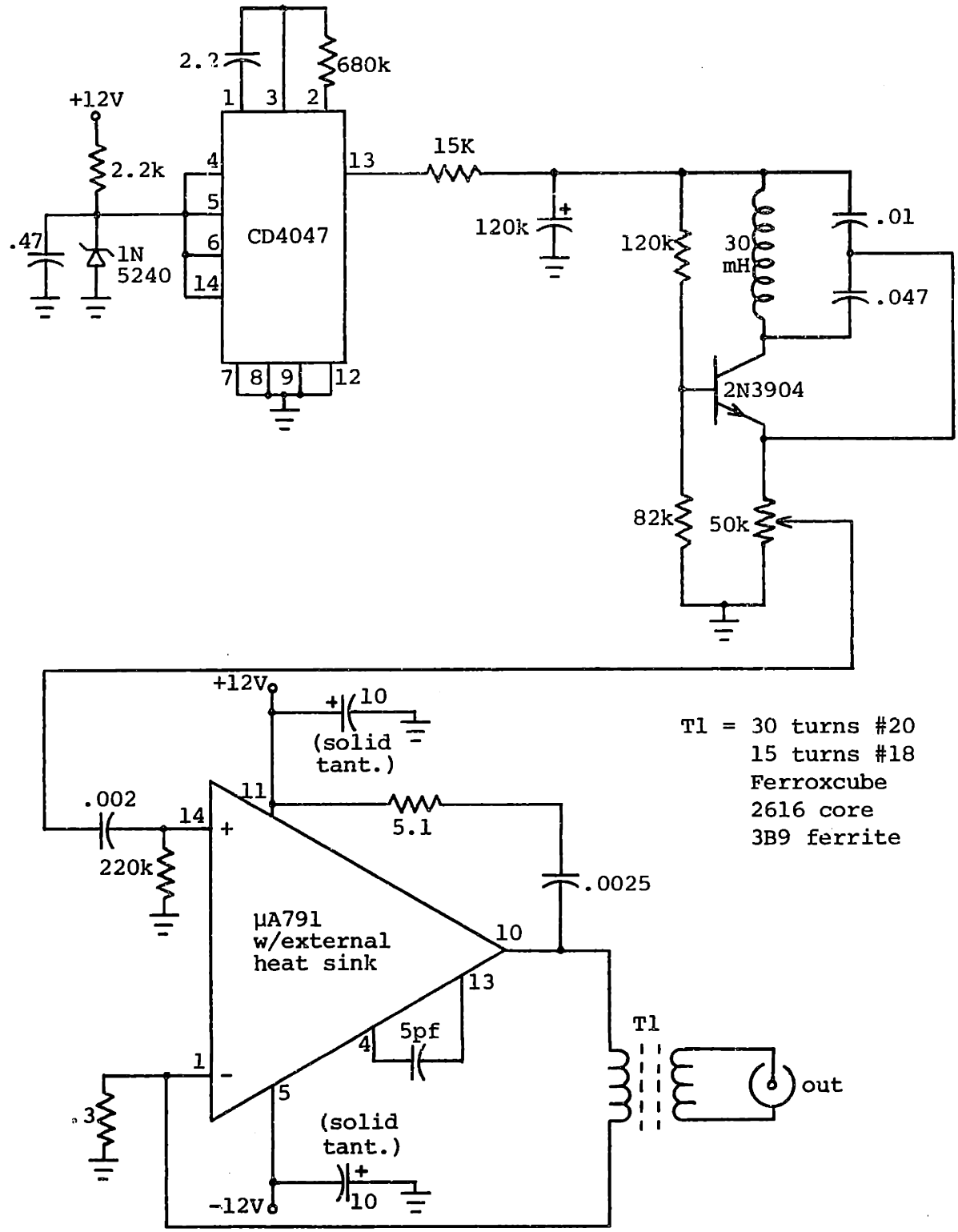

all resistances in ohms, and capacitances in microfarads, unless noted

FIGURE 7.4
10 KHZ TRANSMITTER SCHEMATIC

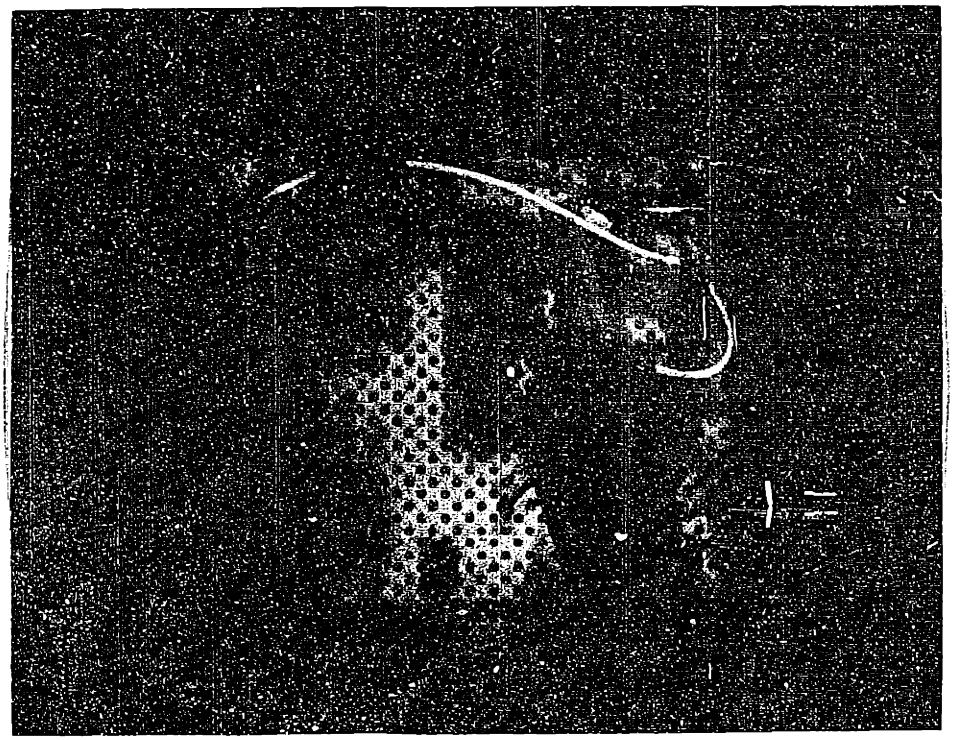

FIGURE 7.5
10 KHZ 1 A R.M.S. TRANSMITTER
(power amp and heat sink are under circuit board)

the same location (the large well in the W.H.O.I. dock), and the result was exactly half the field (in both orientations) that was recorded earlier. As a further test, and to eliminate the possibility of field distortion from the well and a nearby ship, the experiment was performed a third time several days later off the end of the dock and further away from any ships, with identical results.

The value of 4 mhos/m for the conductivity was calculated from temperature and water density data for the first two tests, as was done for the vertical field experiments. Once again, a much closer match between the experimental and theoretical results can be achieved by assuming that the conductivity was actually lower than calculated.

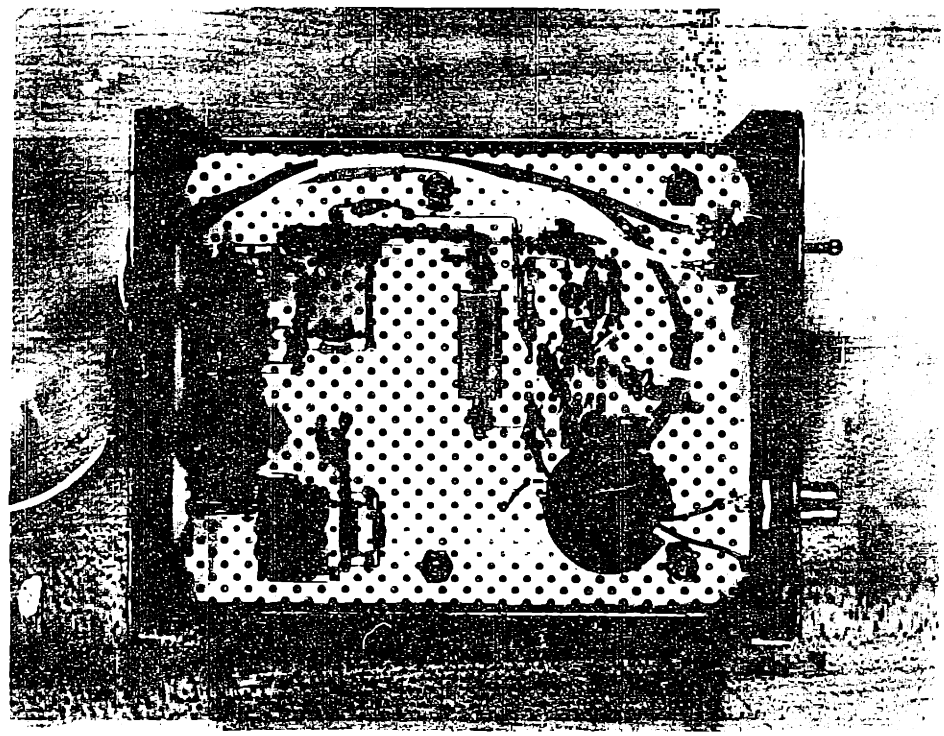

FIGURE 7.5
10 KHZ 1 A R.M.S. TRANSMITTER
(power amp and heat sink are under circuit board)

the same location (the large well in the W.H.O.I. dock), and the result was exactly half the field (in both orientations) that was recorded earlier. As a further test, and to eliminate the possibility of field distortion from the well and a nearby ship, the experiment was performed a third time several days later off the end of the dock and further away from any ships, with identical results.

The value of 4 mhos/m for the conductivity was calculated from temperature and water density data for the first two tests, as was done for the vertical field experiments. Once again, a much closer match between the experimental and theoretical results can be achieved by assuming that the conductivity was actually lower than calculated.

In this case, a conductivity of 3.2 mhos/m gives values of 1.81 mV/m and 1.72 mV/m for the radial and azimuthal fields respectively. This gives a much better fit to the data, but a 20% variation in the conductivity is very hard to believe. The air temperature was quite low on both days when measurements were taken, and it was very windy. This would tend to reduce the temperature and therefore the conductivity of the water at the surface, but it would take roughly a 10°C temperature drop to make the difference measured.[22] Because the tests were done with the two different antenna lengths with identical results, the antenna length must also be discarded as a possible culprit. The quasi-static form of solution developed for the problem should hold over the distances involved without appreciable error, and the other parameters of the system (range, frequency, and permeability) were determined with sufficient accuracy to neglect them as a possible source of error. Any systematic error in the measurements (such as an error in the gain of the preamplifier) should still have produced the same ratio of radial to azimuthal field strength, and certainly not have exchanged the relative magnitudes of the two fields.

The experiment done in 1975 tends to support the accuracy of the radial equation, but the discrepancy between the measured and theoretical values is sufficiently large to prevent any guesses as to whether the radial equation is any more or less accurate than the azimuthal equation. It would have been useful to have compared the two field strengths at several different distances, but deteriorating weather conditions prevented further experimentation.

Even though the theory may not be completely accurate, it is interesting to note that in going from $\sigma = 4$ mhos/m to $\sigma = 3.2$ mhos/m, the ratio of E_{1r} to $E_{1\psi}$ changed from slightly less than 1 to slightly more than 1. This redistribution of the field strengths is dependent on the three parameters f, σ, and r. It may be possible to use this phenomenon to construct a conductivity sensor by varying the frequency (for a fixed geometry) until the two field components are of equal strength. Although calculating the conductivity from the frequency would be complex, this approach should be independent of the electrode contamination problems which most non-inductive conductivity instruments have.

CHAPTER 8

SUMMARY OF RESULTS

A theoretical calculation of the axial field of a vertical dipole antenna was performed using a numerical integration computer program. Experimental measurements of the field at 100 kHz were taken using a submerged transmitter located below the receiving antenna. Although the theoretical curve appears to be about the right shape, the measured field was uniformly stronger than the theoretical field strength by roughly a factor of $1\frac{1}{2}$ to 2, for receiving antenna depths of $\frac{1}{2}$ meter and 1 meter.

It was found that the contribution of the integral to the total field (which consists of the integral term and two Green's function terms) was quite small for transmitter depths greater than a few meters. It should be possible to calculate the field strength for a deeply submerged transmitter by ignoring the integral entirely. The case of a transmitter near the surface communicating with a deeply submerged receiver can then be treated by using the reciprocity theorem.

Ignoring the discrepancy between the measured and calculated values, the attenuation with increasing depth is extremely fast, and it is doubtful that even a very low frequency communications system could be constructed without using very large amounts of power. For the case of a 100 kHz transmission system, an increase in power by a factor of 25 only increases the range by about one meter (at any

range). Measurements were done of the noise spectrum as a function of antenna orientation and depth, with several interesting results. The noise between 1 and 100 kHz is constant with depth and antenna orientation. The noise level decreases only slightly with increasing frequency, despite the more rapid attenuation of propagating high-frequency signals in sea water. The noise was characterized by a constant background level and a number of unidentified stronger narrow-band sources. The background noise level was approximately 20 $nV/m\sqrt{Hz}$ at low frequencies, falling off to about 10 $nV/m\sqrt{Hz}$ at higher frequencies.

Using the computer program developed for the vertical transmission case, the channel capacity was calculated for a communications system using a submerged transmitter and a receiver near the surface. The channel capacity cannot be calculated exactly for this problem because of the frequency-dependent nature of the channel. Simple calculations of an approximate channel capacity show that the loss of average signal power with increasing bandwidth can offset the advantage gained just by increasing the bandwidth, resulting in an overall *loss* in channel capacity for some cases. For this reason, it appears that data transmission at rates higher than a few thousand bits per second may be impractical for ranges greater than a few hundred feet and power levels less than several hundred watts.

Experimental measurements were taken to investigate the relationship between the peak radial and azimuthal fields of a horizontal dipole near the surface. Theory predicts that at short ranges the radial component will be stronger, slowly falling off until

the azimuthal component becomes twice as strong as the radial component as the range is increased.

The experimental results actually indicated that the radial field was slightly stronger than the azimuthal field under conditions for which the theory predicts the reverse. Until this discrepancy can be accounted for, it is difficult to make definite claims about the theoretical predictions. Although it is difficult to come up with an "intuitive" explanation for the change in relative strengths of the two fields, the effect does appear to be real, and may have practical applications for measuring conductivity once the discrepancies between the theory and the measurements are corrected. The general form of the theoretical curve for the radial component matches the data well, supporting the general results reported in the literature, but much more careful measurements will be required to determine the exact nature of the discrepancy.

In general, it is likely (as was suspected) that this method of communication will be limited to a low-frequency, low-data-rate, high-power, short-range system which could probably be easily replaced with an acoustic system unless the acoustic noise environment is exceedingly bad.

Throughout the course of the experiments, all of the measured fields (for three different frequencies, several different orientations, and several different sets of experimental equipment) were stronger than those predicted theoretically by factors varying from 1.5 to 2. Although not enough of an error to make a great deal of practical difference, it does indicate that there is something

amiss. All of the data fit the calculations better if the conductivity was assumed to be somewhat lower than the values calculated from temperature and density data, and it is possible that the "effective" conductivity of sea water may be somehow slightly lower for the kind of electromagnetic propagation measured.

APPENDIX

DESCRIPTION OF COMPUTER PROGRAMS

The equation for the z component of the electric field of a vertical dipole of unit strength is described in Chapter 3. In terms of the capital letter variables used in the APL computer program, the equation is:

$$E_z = \frac{1}{4\pi C}\left\{\left(\frac{\partial^2}{\partial z^2} + iT\right)\left(G_{11} - G_{12} + AV_{11}\right)\right\}, \qquad [A.1]$$

where:

C is the water conductivity in mhos/meter,

$$iT = i\,2\pi F \mu_0 C = k_1^{\,2}, \qquad [A.2]$$

F is the transmitter operating frequency in hertz,

μ_0 is the magnetic permeability of the air and water in henries/meter,

$$G_{11} = \frac{e^{ik_1|h+z|}}{|h+z|}, \qquad [A.3]$$

$$G_{12} = \frac{e^{ik_1|h-z|}}{|h-z|}, \qquad [A.4]$$

$$A = (2\pi F)^2 \mu_0 \varepsilon_0 = k_2^{\,2}, \qquad [A.5]$$

ε_0 is the dielectric constant of air in farads/meter,

-z is the receiver depth in meters,

h is the transmitter depth in meters,

$$V_{11} = \int_0^\infty \frac{2\,L\,e^{-G_1(h-z)}\,dL}{A\,G_1 + i\,T\,G_2} \quad , \qquad [A.6]$$

$$G_1 = \gamma_1 = (L^2 - iT)^{\frac{1}{2}} \xrightarrow[L \to 0]{} -i\,(iT)^{\frac{1}{2}} \quad , \text{ and} \qquad [A.7]$$

$$G_2 = \gamma_2 = (L^2 - A)^{\frac{1}{2}} \xrightarrow[L \to 0]{} -i\,(A)^{\frac{1}{2}} \quad . \qquad [A.8]$$

The electric field can be broken into two parts, which can be written (after taking the indicated partials):

$$E_{z1} = \frac{1}{2\pi C}\left\{ i\,k_1 \left(-\frac{G_{11}}{|h+z|} + \frac{G_{12}}{|h-z|} \right) + \left(\frac{G_{11}}{(h+z)^2} - \frac{G_{12}}{(h-z)^2} \right) \right. \quad , \text{ and} \qquad [A.9]$$

$$E_{z2} = \frac{A}{2\pi C} \int_0^\infty \frac{L^3 e^{-G_1(h-z)}\,dL}{A\,G_1 + i\,T\,G_2} \quad . \qquad [A.10]$$

For the transmitter located beneath the receiver, the distance between the two is:

$$R1 = |h+z| = TD - RD \quad , \qquad [A.11]$$

where TD is the transmitter depth and RD is the receiver depth. The distance between the receiver and the transmitter image is:

$$R2 = |h-z| = TD + RD \quad . \qquad [A.12]$$

If the positive root is chosen for k_1 to ensure decaying exponentials in G_{11} and G_{12}, then:

$$k_1 = (iT)^{\frac{1}{2}} = \left(\frac{T}{2}\right)^{\frac{1}{2}} + i\left(\frac{T}{2}\right)^{\frac{1}{2}} = K1(1+i) \quad . \qquad [A.13]$$

The first step in writing the program was the implementation of a routine to evaluate the value of the integrand (separated into its real and imaginary parts) for any given values of frequency (F), transmitter depth (TD), receiver depth (RD), conductivity (C), and integration variable (L). This routine (called FUNC) is listed below (Program 1):

```
    ∇ FUNC
[1]   T←○2×F×C×1.257E¯6
[2]   R2←TD+RD
[3]   A←((○2×F)*2)×1.1129E¯17
[4]   Q1←((T*2)+L*4)*0.5
[5]   G1←(2*¯0.5)×((Q1+L*2)*0.5),-(Q1-L*2)*0.5
[6]   Q2←(L*2)-A
[7]   DE←(A×G1)+((Q2<0),-Q2>0)×T×(|Q2)*0.5
[8]   NU←((L*3)××¯R2×G1[1])×(2○-R2×G1[2]),1○-R2×G1[2]
[9]   IN←((NU+.×DE),(NU[2]×DE[1])-NU[1]×DE[2])÷DE+.×DE
```

PROGRAM 1
ROUTINE "FUNC"

The first three lines evaluate the variables T, R2, and A in order. Lines [4] and [5] calculate a two-element vector corresponding to the real and imaginary part of G_1 (using the sign chosen in equation [A.7]). Line [6] defines a variable Q_2 equal to G_2^2. Line [7] evaluates the denominator of the integrand (as a two-element vector DE), including choosing either a real or imaginary root of the correct sign for G_2, depending upon the sign of Q_2. Line [8] computes a vector (NU) for the numerator of the integrand after splitting

the exponential into its magnitude and phase components. Line [9] completes the evaluation of the integrand by calculating the real and imaginary parts from DE and NU.

Before this function was integrated, its behavior for various values of F, L, and TD was examined to determine how to perform the integration in as simple and efficient a manner as possible. After examining the integrand (see Chapter 3), a simple trapezoidal integration method was settled on, with the step size (H) and the integration limit (LM) determined by the empirical formulas:

$$H = .005 + .025\,(T)^{\frac{1}{2}} \quad , \text{ and} \qquad [A.14]$$

$$LM = 1 + \frac{12\,(T)^{\frac{1}{2}}}{R2} \quad .$$

The final program (called VFIELD) is displayed below (Program 2):

```
    ∇ MEZ←F VFIELD R
[1]   T←○2×F×C×1.257E¯6
[2]   R1←R[2]-R[1]
[3]   R2←R[2]+R[1]
[4]   K1←(T÷2)*0.5
[5]   E1←(*R1×-K1)×((2○K1×R1),1○K1×R1)
[6]   E2←(*R2×-K1)×((2○K1×R2),1○K1×R2)
[7]   T1←(E2÷R2*2)-E1÷R1*2
[8]   T2←(E1÷R1*3)-E2÷R2*3
[9]   EZ1←(÷○2×C)×T2+(-K1×T1[1]+T1[2]),K1×T1[1]-T1[2]
[10]  A←((○2×F)*2)×1.1129E¯17
[11]  H←0.005+0.025×T*0.5
[12]  LM←1+12×(T*0.5)÷R2
[13]  LI←S←2ρL←K←0
```

```
[14] B:L←L+H
[15]  Q1←((T*2)+L*4)*0.5
[16]  G1←(2*¯0.5)×((Q1+L*2)*0.5),-(Q1-L*2)*0.5
[17]  Q2←(L*2)-A
[18]  DE←(A×G1)+((Q2<0),-Q2>0)×T×(|Q2)*0.5
[19]  NU←((L*3)××-R2×G1[1])×(2○-R2×G1[2]),1○-R2×G1[2]
[20]  IN←((NU+.×DE),(NU[2]×DE[1])-NU[1]×DE[2])÷DE+.×DE
[21]  S←S+(H÷2)×IN+LI
[22]  LI←IN
[23]  →((200>K←K+1)∧L<LM)/B
[24]  EZ←EZ1+(A÷○2×C)×S
[25]  MEZ←(EZ+.×EZ)*0.5
```

PROGRAM 2
COMPLETE VERTICAL FIELD PROGRAM

The program operates as a dyadic function on the frequency F, and a depth vector R = (TD,RD), and returns a number equal to the magnitude of the field at the receiver depth.

Lines [1], [3], [10], and [15] through [20] are taken directly from the routine FUNC, and are used to evaluate the integrand for each iteration of the loop (lines [14] through [23]). Lines [4] through [9] compute the value of E_{z1} given by equation [A.9]. Lines [11] and [12] generate values for the step size and integration limit, and line [13] initializes the variables used in the integration loop. The loop starts at line [14] by incrementing the value of L, then computes the value of the integrand for the new L. Line [21] computes the actual integral of the real and imaginary parts of IN from the present and last value of IN. The value of IN is stored for use in the next iteration by line [22], and line [23] is the branch test used

to continue or terminate the loop. Line [24] computes the total value of the real and imaginary components of E_z, and then line [25] calculates the magnitude of E_z.

REFERENCES

1 Hardy, H. *A System of Short Range Communication by Passing Audio-Frequency Currents Through Water.* Philadelphia: University of Pennsylvania, 1945.

2 Gerke, G. "Feeding the Cat Underwater" *73*, November, 1967, pp. 35 - 36.

3 MacLeod, N. "Electric Diver Communication" *Sea Technology*, May, 1977, pp. 21, 48.

4 Brainard, E. "Underwater Communications System," U.S. Patent No. 3,668,617, June 6, 1972.

5 Rowe, H. "Extremely Low Frequency (ELF) Communication to Submarines" *IEEE Transactions on Communications*, Vol. COM-22, No. 4, April, 1974, pp. 371 - 385.

6 Merrill, J. "Some Early Historical Aspects of Project Sanguine" *IEEE Transactions on Communications*, Vol. COM-22, No. 4, April, 1974, pp. 359 - 363.

7 Warner, K. "The Sarasota Mystery" *Popular Electronics*, March, 1966, pp. 50 - 53.

8 Minto, W. and Faber, J. "Memorandum on Experimental Demonstrations Indicating the Nature and Properties of Hydronic Radiation" Sarasota, Sarasota Research and Development Corporation, 1966 (unpublished).

9 White, D. "Investigation of an Electromagnetic Underwater Communications System" Bachelor's Thesis, M.I.T., 1975.

10 Baños, A. *Dipole Radiation in the Presence of a Conducting Half-Space.* New York: Pergamon Press, 1966.

11 Siegel, M. and King, R. "Electromagnetic Fields in a Dissipative Half-Space: A Numerical Approach" *Journal of Applied Physics*, Vol. 41, No. 6, May, 1970, pp. 2415 - 2423.

12 Siegel, M. and King, R. "Radiation from Linear Antennas in a Dissipative Half-Space" *IEEE Transactions on Antennas and Propagation*, Vol. AP-19, No. 4, July, 1971, pp. 477 - 485.

13 Kong, J., et al. *Field of an Antenna Submerged in a Dissipative Dielectric Medium.* Cambridge: M.I.T., 1977 (unpublished).

14 Cox, R., et al. "The Specific Gravity/Salinity/Temperature Relationship in Natural Sea Water" *Deep Sea Research*, Vol. 17, 1970, pp. 679 - 689.

15 Weyl, P. "On the Change in Electrical Conductance of Seawater with Temperature" *Limnology and Oceanography*, Vol. 9, 1964, pp. 75 - 78.

16 Fessenden, C. and Cheng, D. "Development of a Trailing-Wire E-Field Submarine Antenna for Extremely Low Frequency (ELF) Reception" *IEEE Transactions on Communications*, Vol. COM-22, No. 4, April, 1974, pp. 428 - 437.

17 Burrows, M. "Motion Induced Noise in Electrode-Pair Extremely Low Frequency (ELF) Receiving Antennas" *IEEE Transactions on Communications*, Vol. COM-22, No. 4, April, 1974, pp. 540 - 542.

18 *Non-Government Master Frequency File*, FCC Report Number EFSS10-01.

19 Protasov, V.R. (Excerpts from) "The Language of Fish" *New Life Science Technology*, Series 2, 1968 (unpublished translation).

20 Gallager, R. *Information Theory and Reliable Communications*. New York: John Wiley & Sons, 1968, pp. 407 - 439.

21 Wozencraft, J. and Jacobs, I. *Principles of Communications Engineering*. New York: John Wiley & Sons, 1965, pp. 189, 288, 323.

22 Riley, J. and Skirrow, G. *Chemical Oceanography, Volume 2*. London: Academic Press, Inc., 1975, p. 620.